Characterisation of Titanium Oxide Layers using Raman Spectroscopy and Optical Profilometry: Influence of Oxide Properties

E. J. Ekoi [a*], A. Gowen [b], R. Dorrepaal [b] and D. P. Dowling [a]

**Corresponding author:*
University College Dublin, School of Mechanical and Materials Engineering, Belfield, Dublin 4, Ireland
Email: emmanuel.ekoi@ucdconnect.ie

[a] *University College Dublin, School of Mechanical and Materials Engineering, Belfield, Dublin 4, Ireland*
Email: denis.dowling@ucd.ie

[b] *University College Dublin, School of Biosystems and Food Engineering, Belfield, Dublin 4, Ireland*
Email: aoife.gowen@ucd.ie; ronan.dorrepaal@ucdconnect.ie

Abstract

This study evaluates the use of a combination of Raman spectroscopy and optical profilometry as a surface characterisation technique for the examination of oxide layers grown on titanium metal substrates. The titanium oxide layers with thickness of up to 8 µm, were obtained using a low-pressure oxygen microwave plasma treatment of the titanium metal substrate. The effect of the microwave plasma processing conditions (input power, pressure and treatment time) on the Raman bandwidth, intensity and peak position was evaluated. Also, the effect of these processing conditions on the surface roughness parameters (S_a, S_{dq}, S_{sk} and S_{ku}) of the oxide layers was investigated. Analysis of the peak positions of E_g and A_{1g} modes indicated that the effects of input power and chamber pressure was to induce a shift towards the lower frequency with increasing input power and pressure (1-2 kPa). The intensity of the Raman bands was found to be dependent on the morphology and surface chemistry of the oxide layer. The intensity of Raman band (A_{1g}), was found to be particularly influenced by the average surface roughness (S_a) and the crystallite size. Exponential and polynomial relations were found to correlate with these properties. A two-latent variable Partial Least Squares Regression model developed on Raman spectral data could predict surface roughness with a coefficient of determination (R^2) of approx. 0.87 when applied to the testing of an independent set of titanium oxide test coatings.

Keywords: Titanium Oxidation; Raman Spectroscopy; Surface Roughness Parameters; Raman Intensity; Microwave Plasma; Raman Mapping.

1. Introduction

Raman spectroscopy has been found to be a sensitive characterisation technique for the investigation of complex transition-metal oxides structures, such as those present at either the bulk phase or at a surface [1]. The Raman technique is sensitive to metal-oxide vibrations, which are related to the metal - oxygen bond length as well as its structural environment [1]. This paper investigates the sensitivity of Raman Spectroscopy to changes in the physical features of oxide layers grown on titanium. These oxides are used in applications such as energy capture, medical devices and as catalytic surfaces [2–5].

Titanium dioxide (TiO_2) phases are usually Raman active in the 100 - 900 cm^{-1} region [6–8]. The oxide can exist in three main polymorphs: anatase and rutile, which exhibit tetragonal crystal structure and belong to the space group D_{4h}^{19} and D_{4h}^{14}, respectively. Brookite (orthorhombic), the third polymorph has a lower symmetry than the previous two and belongs to the space group D_{2h}^{15} [9–11]. For brookite, factor group analysis indicates the existence of 69 optical modes with the following irreducible representation of normal vibrations: $9A_{1g} + 9B_{1g} + 9B_{2g} + 9B_{3g} + 9A_{1u} + 8B_{1u} + 8B_{2u} + 8B_{3u}$ [12]. 36 of the predicted modes represented by A_{1g}, B_{1g}, B_{2g} and B_{3g} are active in Raman whereas the rest are active in infrared except for the A_{1u} mode which is inactive in both Raman and infrared [12]. For anatase, there exists 15 optical modes with the normal vibrations: $1A_{1g} + 1A_{2u} + 2B_{1g} + 1B_{2u} + 3E_g + 2E_u$ [13]. Six of the modes represented by $1A_{1g}$, $2B_{1g}$, $3E_g$ symmetries are Raman active [7]. In rutile, the two TiO_2 units in the unit cell implies 15 vibrational modes. These modes belong to the following irreducible representations [7,8]: $1A_{1g} + 1A_{2g} + 1A_{2u} + 1B_{1g} + 1B_{2g} + 2B_{1u} + 1E_g + 3E_u$. Rutile has four Raman active modes with symmetries: B_{1g}, E_g, A_{1g} and B_{2g} [7]. Several authors have investigated the Raman vibration modes of anatase and rutile TiO_2 [8,14–22]. It has been reported that molecular bonds make different contributions to the Raman-active modes (by influencing the intensity of the Raman modes), depending on the crystal planes present [8,14,22]. The E_g, B_{1g} and the A_{1g} Raman modes are mainly associated with the symmetric stretching vibration, the symmetric bending vibration and the anti-symmetric bending vibration of O-Ti-O, respectively [14,18]. The intensities of these Raman vibration modes are dependent on the oxide's crystallinity, which can be altered during oxide formation due to furnace treatment parameters such as pressure and temperature [8,14]. For example, the vibrational modes (A_{1g} and E_g) of rutile TiO_2, have been shown to exhibit systematic Raman shifts, broadening and intensity reductions as the crystallite size decreased; effects attributed to a three-dimensional phonon confinement [17]. Li Bassi *et al.* [21] observed a correlation between Raman peak at 144 cm^{-1} (E_g mode) shift and crystal size of anatase TiO_2 nanoparticles (< 40 nm). The observed Raman shift to lower wavenumber with increasing crystal size

(particularly for sizes less than 10 nm) was interpreted based on a phonon quantum confinement model. Yan *et al.* [14] observed that the ratios between different Raman vibrational modes (A_{1g}/E_g and B_{1g}/E_g in anatase and A_{1g}/E_g in rutile) were approximately the same. However, for a mixed phase structure, the ratio of the integrated Raman peak intensity of rutile peak at 446 cm^{-1} (E_g) to that of anatase at 396 cm^{-1} (B_{1g}) has been suggested to yield a semi-quantitative measure of the weight ratio of rutile to anatase [23,24].

In this study TiO_2 is grown by controllably oxidising the pure titanium metal using an oxygen plasma treatment. In previous studies the use of both physical and chemical treatments has been investigated for this oxidation [25–31]. The physical methods include the use of thermal treatment, thermal spraying, physical vapour deposition and ion implantation techniques, while the chemical oxidation methods include the use of sol–gel treatment, electrochemical treatments (anodic oxidation) and chemical vapour deposition (CVD) [2]. For example, Zwilling *et al.* [32,33] obtained oxide-layers with structure and morphology either compact and thin (less than 20 nm), or porous and thick (more than 50 nm depending on the electrolyte used) using electrochemical treatments. In addition to conventional chemical treatments, there have also been a number of reports on the use of plasma treatments for the oxidation of titanium [34–36]. Plasmas have the advantage of speed of oxidation, with treatment times reduced from hours in conventional chemical treatments to seconds or minutes. For example, exposure to a DC plasma yielded titanium oxide layer thicknesses of 30 nm, after 5 minutes' treatment [34]. Microwave plasma discharges are usually more effective than DC plasmas, because of the higher density of atomic oxygen that can be generated using this type of discharge; and they can be operated in a wide gas pressure range [36].

This study investigates how Raman spectra are influenced by the physical and surface chemistry of titanium oxide layers, obtained using low-pressure microwave plasma oxidation treatments under three process conditions (input power, pressure and treatment time). Of particular interest is to investigate how the grown oxide surface roughness parameters (S_a, S_{dq}, S_{sk} & S_{ku}), oxygen concentration and crystallite size influence the intensity of the associated Raman band.

2. Materials and Methods

A microwave Circumferential Antenna Plasma (CAP) reactor operating at 2.45 GHz was used for the plasma oxidation treatment of titanium substrates. The CAP system is described in detail elsewhere [37]. Commercially pure (CP) titanium blocks (250 mm x 150 mm x 8 mm) were faced and cut into discs

(diameter 25 mm and thickness 5 mm), using a Hurco VM3 CNC mill system. These discs were ground and polished to a mirror finish using silicon carbide abrasive paper (240, 320, 600 and 800), diamond suspension (6 and 3 μm) and colloidal silica. They were subsequently cleaned in an ultrasonic bath using methanol and deionised water; then blow-dried with air prior to plasma treatment. The microwave plasma process involved a five-minute pump down to a base pressure of 8 Pa, before the introduction of oxygen into the chamber. The pressure was allowed to rise to 0.6 kPa, before igniting the microwave discharge. The titanium disc was mounted in the plasma using a molybdenum metal holder, which in-turn was supported on a quartz rod. The processing conditions were systematically altered with input powers in the range 0.9 to 2.1 kW, operating pressures between 1.0 and 5.0 kPa and treatment time between 5 and 25 minutes. Single test coupons were evaluated under each processing condition. The oxygen gas (99.9%) flow rate was maintained at 100 sccm for all treatments. After each treatment, the sample was left in oxygen and vacuum atmosphere for 3 and 2 minutes, respectively, before chamber ventilation.

Temperature measurements were carried out using a LASCON QP003 and LPC03 ratio pyrometers from Dr. Mergenthaler GmbH & Co. KG. The temperature generated on the titanium substrate by the discharge was found to be in the range 716 to 910°C, depending on the plasma processing conditions used.

The morphology of the resulting titanium oxide-layer samples was characterised using a FEI Quanta 3D FEG DualBeam scanning electron microscope (SEM) and cross-section analysis of the oxide layer thickness obtained using a focused ion beam (FIB). Energy-dispersive X-ray spectroscopy (EDX) operating at 15 kV was used to obtain elemental data at five different points on each sample. For EDX measurement validation, two different EDX systems (20 mm^2 Oxford Inca and 30 mm^2 Oxford AZtecOne EDX detectors) were used to obtain the elemental information. Similar results were obtained from these systems. Surface roughness measurements were obtained using both a Bruker's NT1100 and NPFLEX 3D optical profilometers in vertical scanning interferometry (VSI) mode. The titanium test substrates were found to have a roughness (S_a) of 0.01μm.

The phase composition and crystallinity were determined using Siemens D500 XRD system and an inVia Micro-Raman confocal spectroscopy system (Renishaw, Wotton-under-Edge, Gloucestershire, UK). The XRD system operated at 40 kV and 30 mA at a wavelength of 0.1541 nm (CuKα radiation). The scan wavelength for this system was in 2θ mode with a scanning range from 20° to 80° with steps of 0.02° per second. The average crystallite size of the samples treated with various input power, pressure and time was estimated from the most intense (110) XRD peak using the Scherrer equation [38,39]: $\tau = (k\lambda)/ (\beta$

cos θ), where τ is the crystallite size, k is the shape factor with a value of 0.9 (assuming spherical crystallites), λ is the X-ray wavelength, β is the line broadening described by the full width at half-maximum (FWHM) peak height in radians (where $\beta_{Structural} = \beta_{Observed} - \beta_{Standard}$), and θ is half of the Bragg angle (in radians). Lanthanum hexaboride (LaB_6) was used as the standard for instrument broadening.

Raman scattering was recorded using a laser of wavelength 532 nm with a maximum laser power of 2.25 W. A 10x 0.25NA objective lens was used to focus the laser beam on the sample surface for an exposure time of 10 seconds each time. Spectra were calibrated to a silicon shift at 520 cm^{-1}. The detector used was a NIR enhanced Deep Depletion CCD array (1024 × 256 pixels) which was Peltier cooled to -70°C. A 1800 lines/mm grating was used for all the Raman scans. Point spectra were obtained using the "Extended" scan option in this system, resulting in spectra in the Raman shift range of 22 - 1806 cm^{-1} measured over 1015 spectral data points with an average spectral step size of 1.75 cm^{-1}. Baseline correction and curve fitting of the Raman spectra was carried out using WiRE StreamLineHR image acquisition software and MATLAB. Raman maps were acquired using the same system in "static mode" at 100% power, which resulted in a slightly different spectral range of 90 - 1860 cm^{-1} with a mean spectral size of 1.75 cm^{-1} over 1015 measured spectral bands. An area corresponding to 4x4 mm at the centre of sample 3 was mapped. Spectra were acquired at steps of 50 µm in the X and Y mapping directions. The exposure time per pixel was 1s, and the total acquisition time was approximately 100 minutes.

2.1 Partial least squares regression

Non-Linear Iterative Partial Least Squares (NIPALS) regression [40] was used in order to predict measured surface roughness from the Raman spectra. The model was trained and calibrated using Raman spectra from five samples and then tested on an independent validation set of spectra from five separate TiO_2 coatings. The trained PLS regression vector was applied to the full NIR images and compared with the k-means results. In order to remove the baseline effects, a second derivative Savitsky Golay pretreatment was applied to the Raman spectra.

Prior to model development the point spectra and mapping data were trimmed to the Raman shift range 100 - 1086 cm^{-1} and the mapping data were interpolated to match the exact Raman shifts of the point spectra. In addition, differences in Raman peak intensity due to the use of the "extended" scan mode in the spectral acquisition and "static" scan mode in the map acquisition were removed by scaling the Raman map data to the ratio of mean Raman spectra of static and extended modes at 506 cm^{-1}.

3. Results and Discussion

In this work, the influence of microwave plasma processing conditions of input power, chamber pressure and treatment time on the roughness and Raman spectra of the oxide layer obtained were systematically investigated. The input power processing condition was investigated in the range of 0.9 to 2.1 kW at a pressure and treatment time of 4.6 kPa and 10 minutes, respectively. A pressure in the range of 1 to 5 kPa was investigated at a constant input power and treatment time of 1.2 kW and 10 minutes, respectively. Finally, the influence of treatment time was investigated in the range of 5 to 25 minutes at constant input power and pressure of 1.2 kW and 4.6 kPa, respectively.

As shown in Figure 1 the oxygen microwave plasma oxidised metal exhibits a highly porous morphology both at the surface and in the bulk of the oxide. Examination of the oxide layer revealed that it was composed of a less porous structure in the lower region and a columnar porous structure in the upper region. The morphology was mostly influenced by high input power and pressure. For instance, at an input power and pressure of 0.9 kW and 1 kPa, respectively, the oxide films were relatively compact. This morphology is different from what would be obtained in a conventional furnace treatment in that it exhibited a relatively rough structure, with large grains. This is in contrast to that reported for furnace oxidation treatments of titanium, where the more slowly grown oxide exhibits a much denser morphology, with little or no porosity [36]. A possible explanation is that the first stage of the oxidation process involves the adsorption of oxygen on the titanium surface as a function of the available oxygen species [41]. Compared to air furnace treatment, microwave plasma oxidation is more effective because of the higher density of oxygen species that can be generated. Associated with this level of oxygen species is the high rate of bombardment of the growing film by oxygen species obtainable. It has been reported previously that the energy impacted to the substrate by the plasma electrons/photons leads to the excitation and mass transport of metal ions towards the surface [42]. It is also reported that there is a build-up of electrons at the metal surface such that a negative potential is raised, and thus, this attracts positive ions to the surface to form neutrals [43]. These oxygen neutrals can react with Ti ions to form oxide nuclei. Depending on the input power and pressure used during treatment, the number density of oxygen atoms in the plasma lead to either the creation of high or low number of nucleation sites [44]. It is likely that the nucleation density controls both the roughness and the porosity of the titanium-oxide layer formed on the titanium substrate by inducing a Volmer-Weber type of growth mode [45] in which the oxide nuclei grow as islands until coalescence occurs. At low input power and pressure, a dense oxide structure which reduces the diffusion of the Ti^{n+} ions through the growing oxide

layer to the oxide-plasma interface is obtained. However, with increasing input power and pressure, a change in the oxide structure; as evidenced by the dominant vertical growth of the grains at the top regions of the oxide, is observed. It can be observed that as the thickness of the oxide layer increased, there appeared to be a critical thickness (influenced by porosity level) above which a more porous structure is observed (Fig. 1). The difference in the grain structure of the bulk and top regions of the oxide layer may have become necessary due to the dense nature of the bulk oxide. It has been reported by other researchers who used microwave plasma system to grow diamonds that it is possible that not all the grains which were formed during nucleation survived to reach the surface due to a van der Drift type of competition [44]. Only the grains which grew perpendicular to the substrate surface would survive. Others would be buried during the growth process further limiting diffusion. This would account for the differences in the oxide layer structure observed during microwave oxygen plasma oxidation. A typical schematic mechanism on how the oxygen microwave plasma process induced high porosity in the oxide film is given in Fig. 2. Another observable feature of the microwave plasma obtained oxide is the presence of well-defined crystal facets. The thickness of the oxide layer shown in Fig. 1 is about 10 µm**.** This thick oxide was grown in 10 minutes using an input power and chamber pressure of 2.1 kW and 4.6 kPa, respectively.

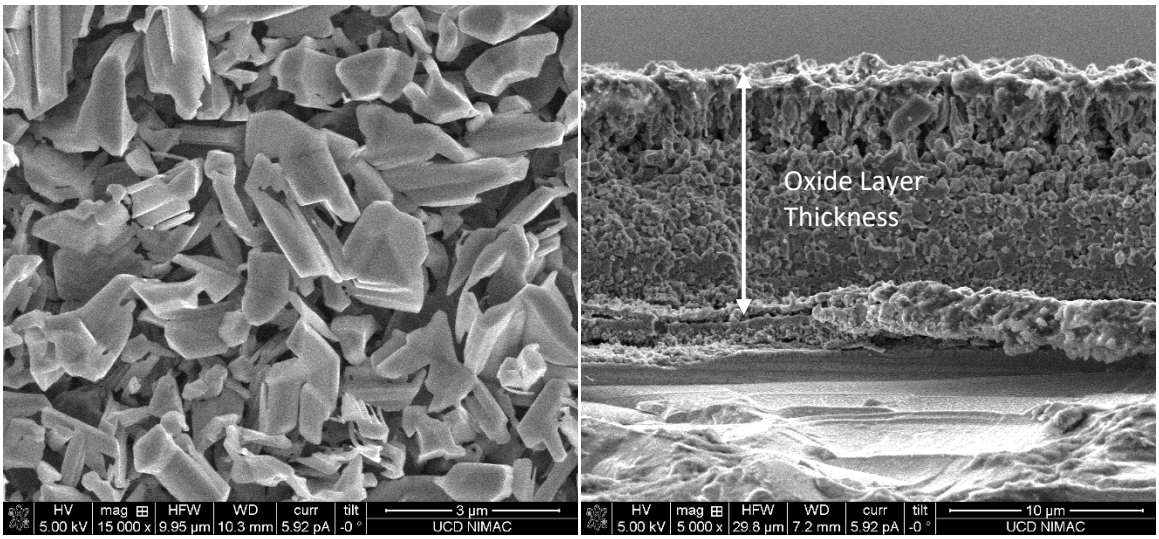

Figure 1: SEM images of a typical morphology and thickness of oxide grown in an oxygen microwave plasma. The thickness and growth temperature of the oxide layer were 9.89 µm and 910 °C, respectively.

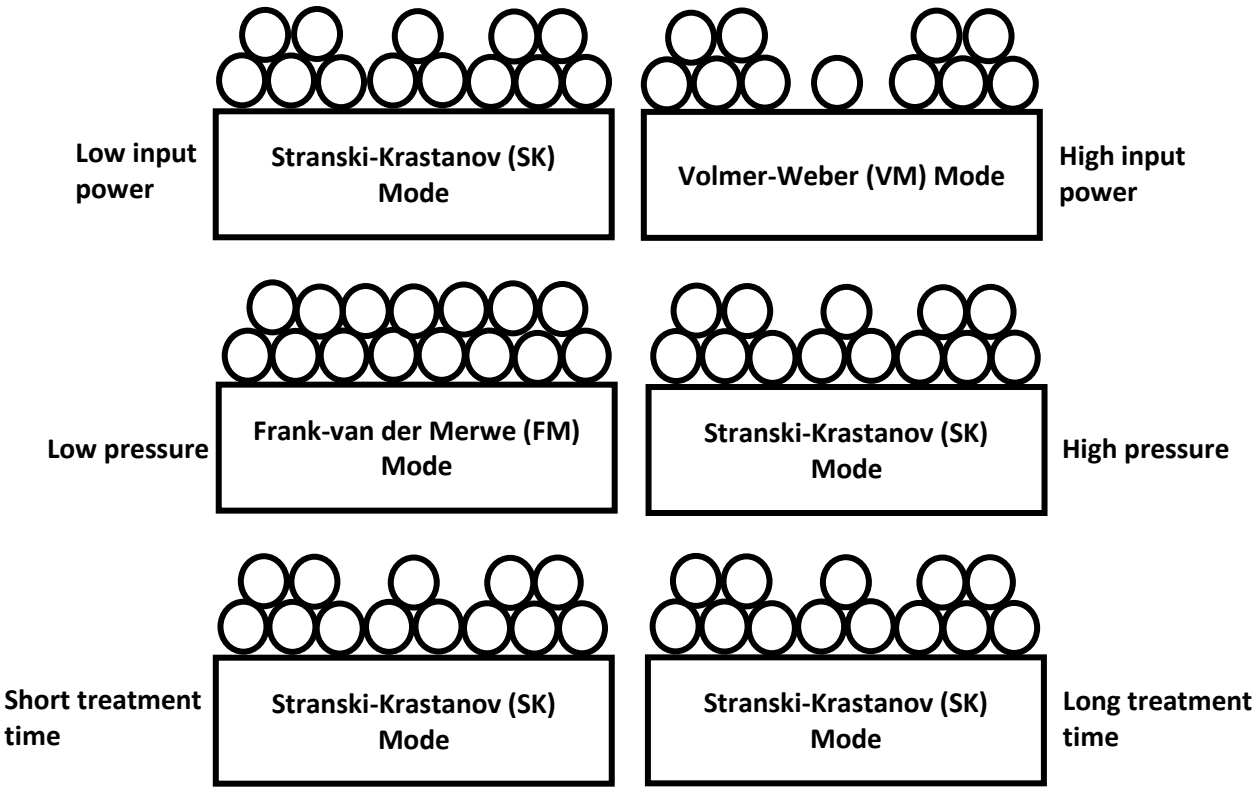

Figure 2: A typical schematic mechanism on how oxygen microwave plasma processing conditions induce porosity in the oxide film.

3.1 Effect of Microwave Plasma Processing Conditions on the Phase Composition, Raman Peak Position and Linewidth of Oxide Layers

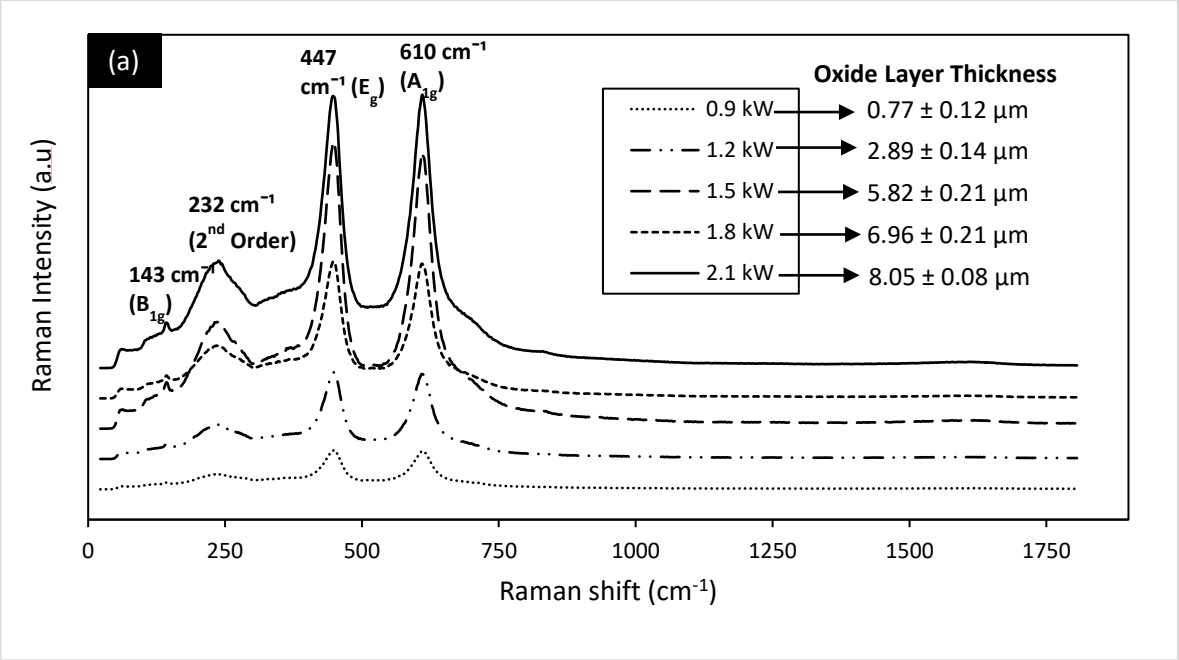

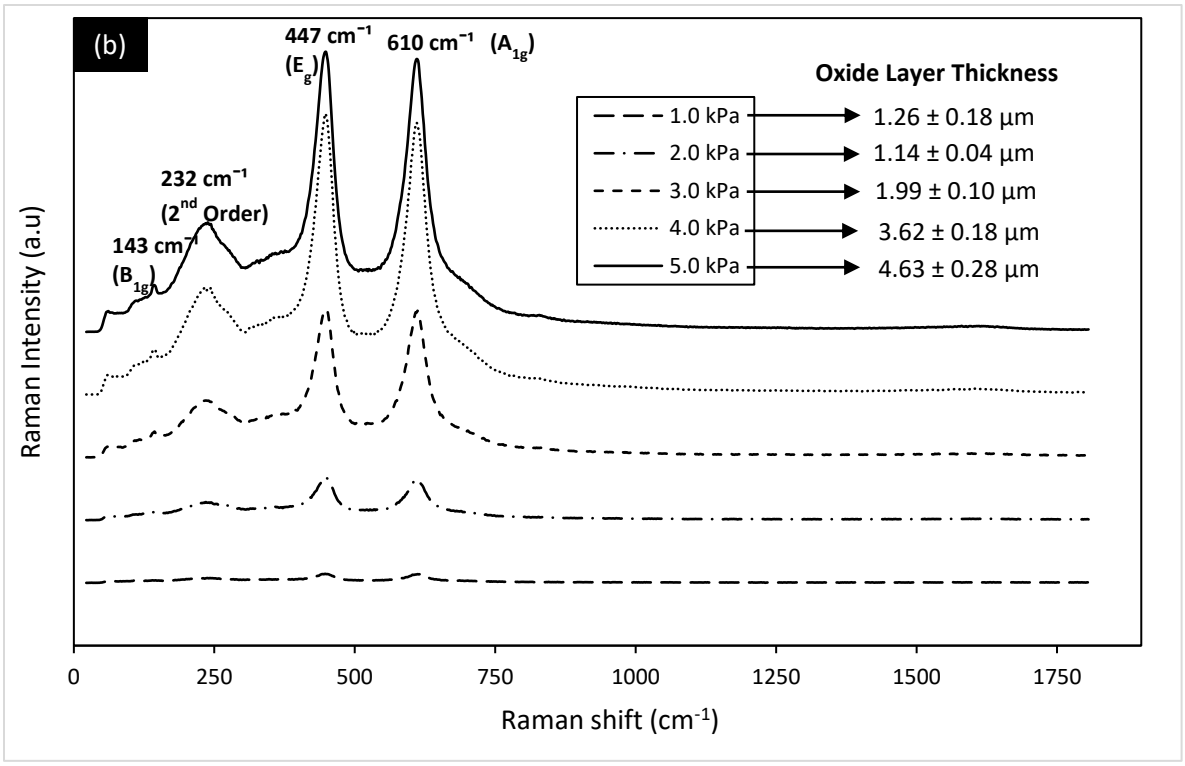

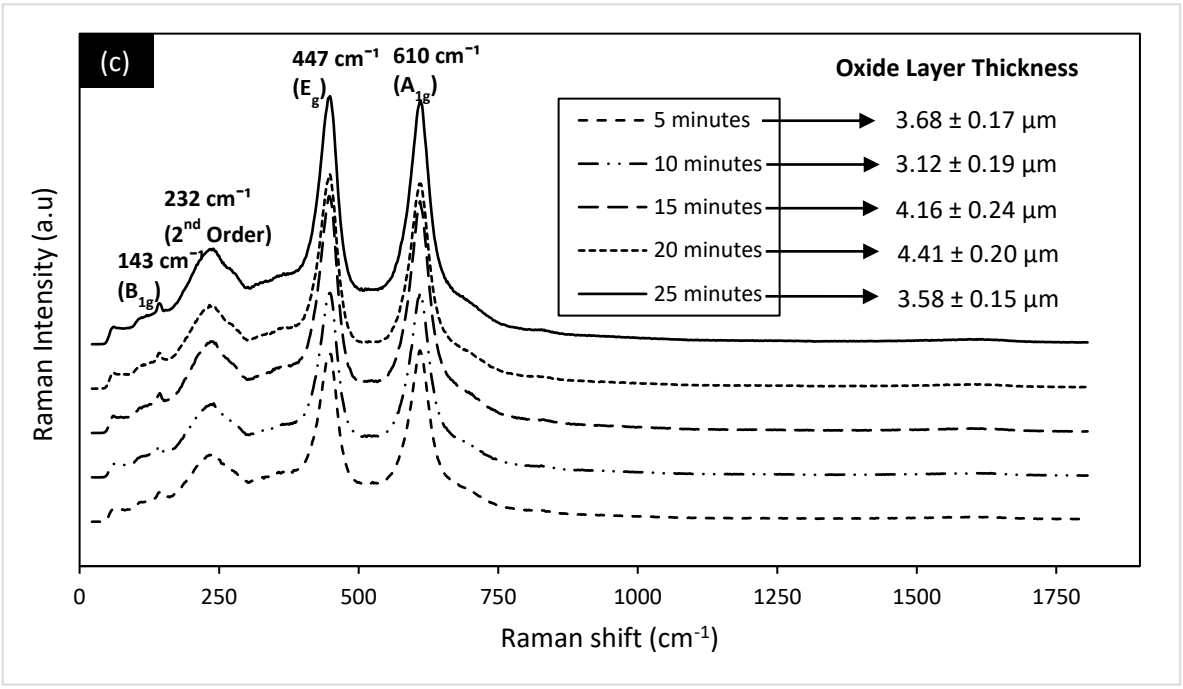

Figure 3: Raman spectra of samples treated at: (a) input power of 0.9 – 2.1 kW; (b) pressure of 1.0 to 5.0 kPa; (c) treatment times of 5 to 25 minutes.

Figure 3 shows the Raman spectra of TiO_2 layer grown with the various microwave plasma processing conditions discussed in section 3. The thickness of the oxides grown at the various processing conditions is also shown. As can be observed, the thickness generally increased with increased input power and pressure. The thickness of the oxide layers increased for treatment times of 10 to 20 minutes. Above 20 minutes treatment period, a reduction in thickness was observed. This reduction in thickness may indicate "oxide thickness saturation" [36]. It has been reported that rutile crystal exhibits dominant peaks at 446.6 and 609.8 cm^{-1} [36] (This is supported by the XRD results of Fig. 4 which confirms that the oxide phase was mostly that of rutile). These Raman peaks have been assigned to two of the four Raman active modes of rutile single crystal (E_g and A_{1g} respectively). The intense E_g peak supports the increasing crystallinity of the samples as the treatment conditions are altered. The sharp low-frequency line at 143.2 cm^{-1} and the weak high-frequency line at 800.27 cm^{-1} are assigned to the remaining of the four active modes (B_{1g} and B_{2g} respectively). The peak at 800.27 cm^{-1} is the weakest and can only be observed on some sample profiles. The peak became more pronounced with increase in input power from 0.9 to 2.1 kW and treatment pressure from 1.0 to 5.0 kPa (Fig. 3 (a) and (b), respectively. There was no significant change observed in the intensity of this peak for samples processed in the range of 5 to 25 minutes plasma treatment time. The broad peak at 232.4 cm^{-1} may be attributed to either disorder induced scattering or second-order effect [46], which is a result of multi-phonon processes. It was noted that this peak became more intense for the oxide layers deposited at higher input power and chamber pressures. This effect, however, was not found to correlate as strongly with changes in plasma treatment time (Fig. 3 (c)). For samples grown using input power in the range of 0.9 – 2.1 kW, there was a 1-fold increase and decrease in the linewidth of E_g and A_{1g} bands, respectively, with increasing input power. For samples processed in the range of 5 to 25 minutes, both E_g and A_{1g} band linewidths decreased by 1-fold. A typical example of the effect of processing conditions on the E_g and A_{1g} band widths is given in Fig. 5 and shows the influence of pressure on the band widths. In this case, the linewidths decreased and increased for E_g and A_{1g} bands, respectively, as the pressure changed from 1 kPa to 2 kPa. It has been suggested that peak broadening occurs due to nanocrystallinity and phonon confinement effects, and that there was a characteristic dependency between grain size and peak position and broadening in Raman analysis [47–49]. Analysis of the peak positions of E_g and A_{1g} modes indicates that the effects of input power and chamber pressure was to induce a shift towards the lower frequency with increasing input power and pressure (1-2 kPa) (Figs. 6 & S1). However, as the pressure increased to the range of 3 to 5 kPa, there was no significant redshift observed (Fig. S1). Samples processed for 5 to 15 minutes induced a slight shift towards the higher frequency for the E_g

band; whereas for the A_{1g} band, there was no significant effect on the Raman peak positions. For samples processed using more than 15 minutes, both the E_g and A_{1g} bands exhibited a redshift (Fig. S2). The spectra obtained from titania coatings from this work are also compared to previous results in Table 1 [9–11,36]. As shown in Table 1, there is good agreement with examples of previous reports in the literature.

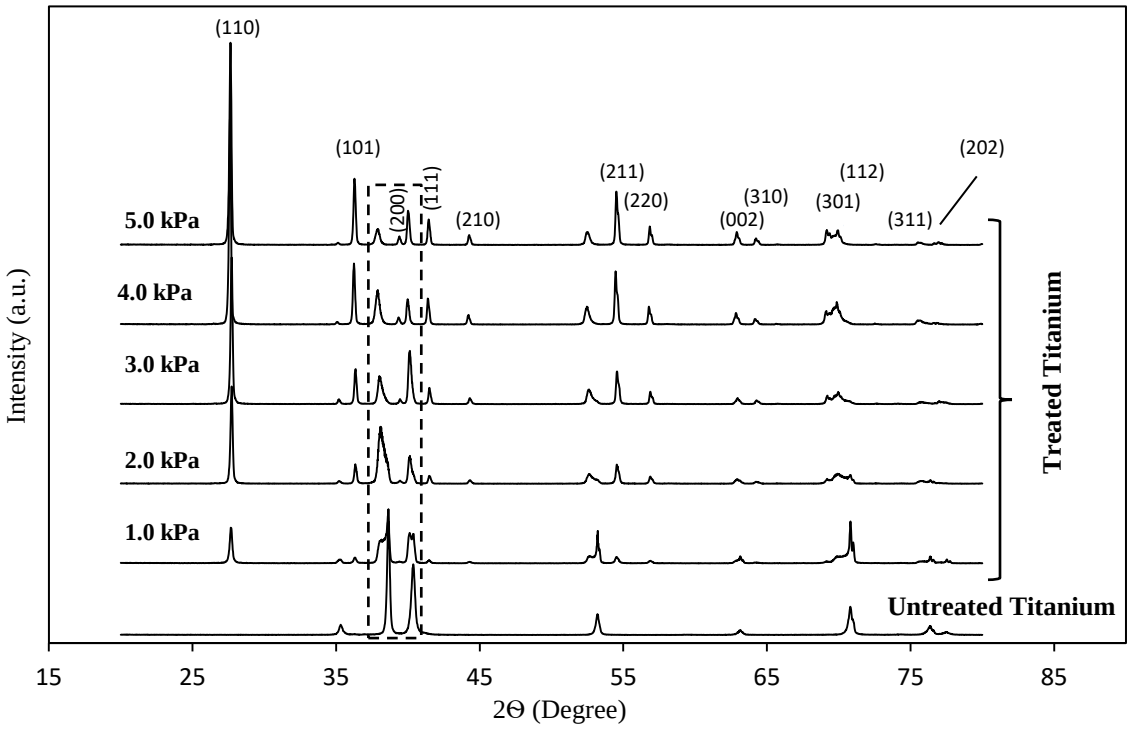

Figure 4: XRD diffraction patterns obtained for untreated and plasma oxidised titanium using microwave plasma pressure of 1 kPa – 5 kPa. The peaks indicate a Rutile phase of TiO_2.

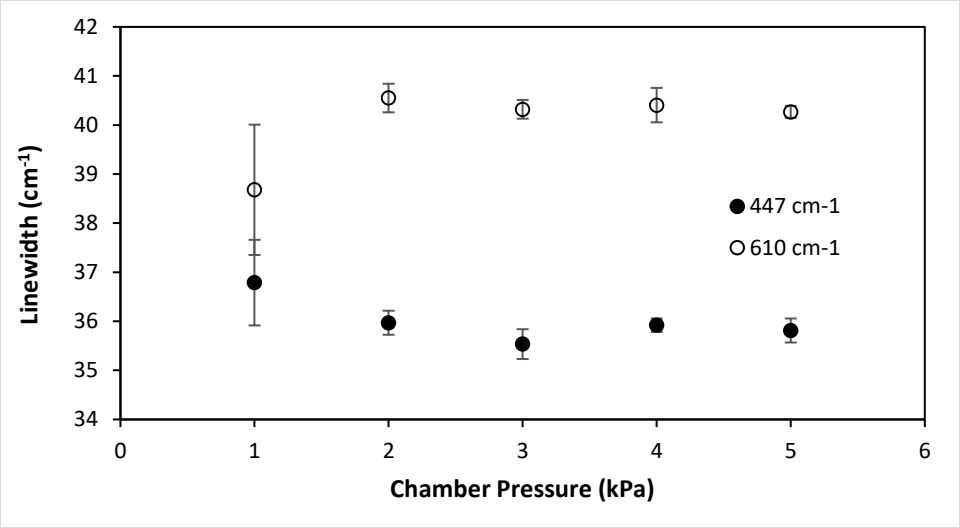

Figure 5: Influence of pressure on the linewidth of the E_g (447 cm^{-1}) and A_{1g} (610 cm^{-1}) bands.

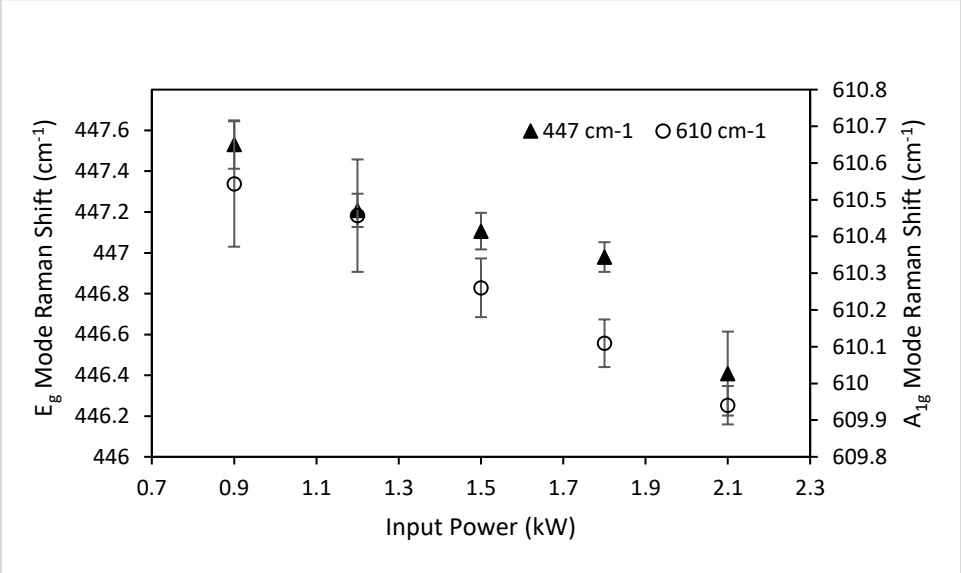

Figure 6: Effect of input power on the position of the peaks for the E_g (447 cm^{-1}) and A_{1g} (610 cm^{-1}) Raman bands.

Table 1: Comparison of the Rutile band obtained in this study with works from other researchers.

This Study & Ekoi *et al.* [36]	**Ma *et al.*** [9]	**Arsov *et al.*** [10]	**Assigned Mode** [11]
143.2 ± 0.3	140.2	143	B_{1g}
232.4 ± 0.9	235.5	236	Multi-phonon process
446.6 ± 0.3	445.8	447	E_g
609.8 ± 0.4	609.8	612	A_{1g}
-	825.5	826	B_{2g}

In order to investigate further the structure, phase composition and transformation in the oxides as a function of processing conditions, XRD profiles of the region enclosed in rectangle in Fig. 4 is presented in Fig. 7 and depicts the influence of pressure on the oxide phase composition and transformation. The observed peaks in the diffraction profile between 37 and 41° (using JCPDS-ICDD card numbers 10–63, 11–217, 11-218, 11–474, 18–1401, 18-1402, 18-1403, 18-1404, 21-1272, 21-1276, 23-606 and 40-806) suggest the presence of phases different from rutile. The presence of Ti_2O, Ti_3O_5 and some members of the homologous series Ti_nO_{2n-1} (where n is a number between 4 and 10) [50] phases was observed. Phase transformation could be observed with increasing chamber pressure (2 – 5 kPa). The double peak structures observed between 37 and 41° for samples treated at a pressure of 1.0 kPa in Fig. 7 represent mixed phases of titanium metal, Ti-O solid solution and other phases which with Rutile, Ti_2O, Ti_3O_5 and some members of the homologous series Ti_nO_{2n-1} becoming the dominant phase with increasing pressure in this region. These phases would influence the level of conductivity and semiconductor-to-metal transitions in the oxide layers [50,51]. Similar results were obtained when input power and treatment time were varied while other parameters remained constant, however, mixed phases of titanium metal and Ti-O solid solution were absent at the lowest treatment conditions (See Figs. S3 & S4). It can be observed that in all the samples treated, the peaks representing the mixed phases decreased with increasing input power, pressure and time indicating a transition in phase from a mixed phase to that of purely rutile phase structure (Figs. 4, S3 & S4). The implication of the phase transition as a function of process conditions is a transition from a defect structure dominated by the Magnéli phases to one mostly containing point defects such as oxygen vacancies and titanium interstitials [52–54]. The presence of oxygen vacancies at the oxide surface would influence the adsorption of molecules [54].

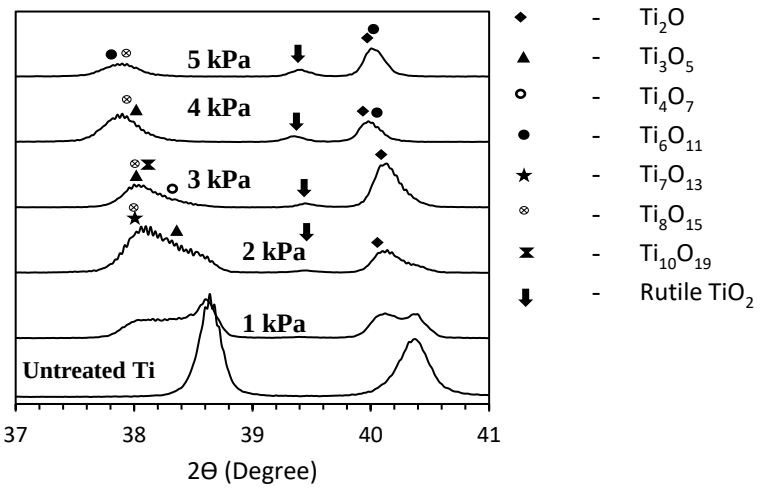

Figure 7: Region in the XRD profile of Fig. 4 showing the oxide phase transformation with the increase in pressure from 1 kPa during plasma oxidation treatments.

3.2 Influence of Processing Conditions on the Oxygen Concentration and Intensity of the A_{1g} Raman Band

Figure 8 shows a typical morphology of oxide layers grown at various microwave plasma processing conditions. As can be seen, grain size and porosity progressively changed with increased input power and pressure. The change in the oxide structure may be related to the oxygen concentration in the growing oxide layer as a function of microwave plasma processing conditions. A typical example of the influence of pressure on the oxygen concentration (determined using EDX analysis) and the Raman spectra intensity of the A_{1g} band is shown in Fig. 9. It must be noted that although two different EDX measurement systems were used to characterise, verify and validate measured oxygen concentration in these oxides, the O/Ti ratio was in the range of (1.92 ± 0.04 to 2.22 ± 0.05), (2.30 ± 0.03 to 2.18 ± 0.06) and (2.33 ± 0.03 to 2.37 ± 0.04), respectively, for pressure, input power and treatment time processing conditions. A Possible reason could be the presence of excess oxygen in the oxide structure which would result in the formation of interstitial oxygen [55,56]. This could be observed in Fig. 9 where at a pressure of 1 kPa, the O/Ti ratio was about 1.92, however, above this pressure, the ratio was 2.23. The explanation is that at higher oxygen pressure, there are more oxygen species bombarding the film; and more oxygen condensed onto the oxide film when the microwave plasma source was turned off after treatment [55,56]. The effect is the formation of interstitial oxygen which could have combined with the lattice oxygen to form either a substitutional or interstitial O_2 [56–58]. This would result in either oxide

crystal lattice strain due to the slight outward movement of the neighbouring Ti atoms or oxygen vacancy defects [55–57]. The observed Raman intensity trend as a function of pressure may be related to the number of Ti-O molecules available for excitation during Raman scan as discussed above. Similar results were obtained for samples investigated using input power and treatment time conditions (Figs. S5 & S6).

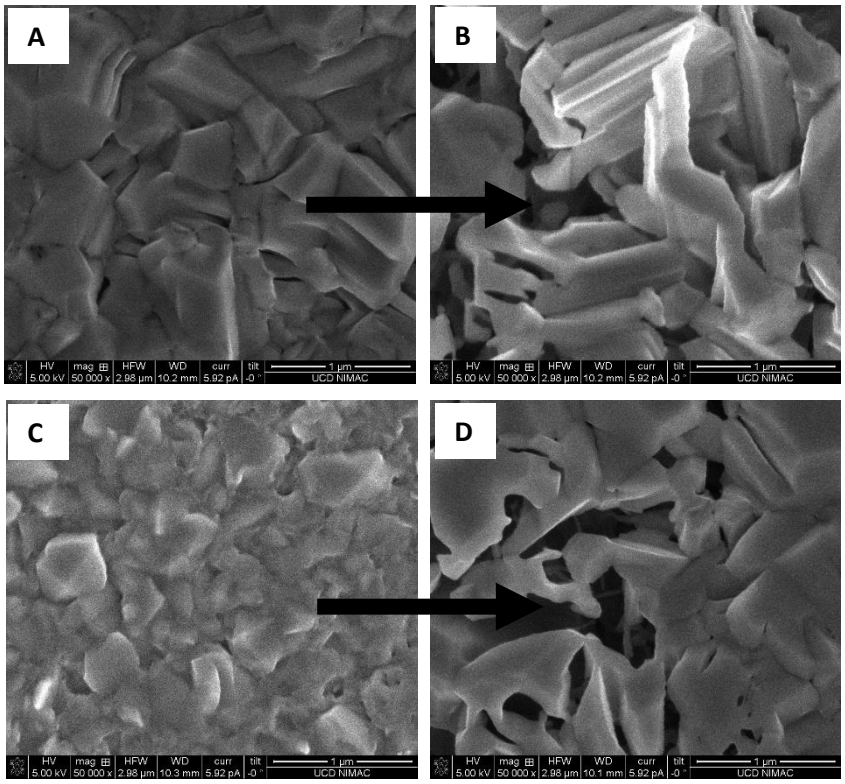

Figure 8: Typical SEM images of oxidised layers demonstrating the influence of increased input power and chamber pressure on oxide morphology and pore structure: (A) 1.2 kW; (B) 2.1 kW; at a fixed pressure of 4.6 kPa, (C) 2.0 kPa; (D) 5.0 kPa at a fixed input power of 1.2 kW.

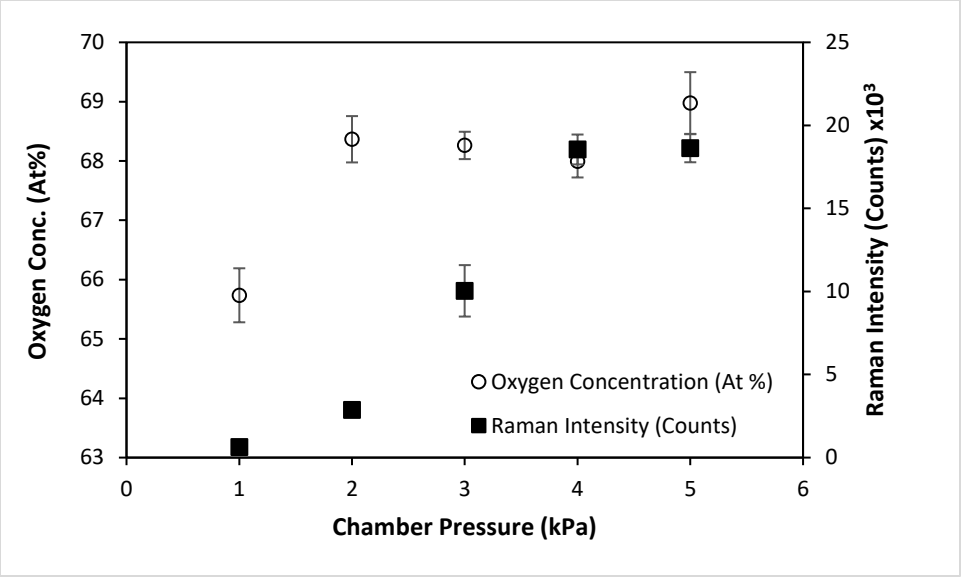

Figure 9: Effect of processing pressure on the oxygen concentration (At % weight) and the intensity of the A_{1g} Raman band.

3.3 Influence of Crystallite Size on Raman Peak Position and Intensity

The crystallite size of the oxides was estimated from the XRD profile of the samples, using the Scherrer's equation. The 110 XRD peak of TiO_2 was used for this estimation. The estimated crystallite sizes obtained were plotted against the Raman intensity of the A_{1g} band. The result is presented in Fig. 10. There appears to be a correlation between the crystallite size and the intensity of the Raman spectra obtained. This plot was carried out without consideration of the microwave plasma treatment conditions used to obtain the oxides. It was observed that the Raman peak positions of A_{1g} and E_g bands exhibited a strong correlation with the oxide crystallite size as demonstrated in Figure 11. The peak positions tend to shift towards lower wavenumbers with increasing crystallite size. A similar correlation between Raman peak at 144 cm^{-1} (E_g mode) shift and crystal size was observed by Li Bassi *et al.* [21] for anatase TiO_2 nanoparticles (< 40 nm) and interpreted based on a phonon quantum confinement model. The red shift of the E_g rutile mode has been reported to be a result of the nonstoichiometric effects for TiO_2 nanophase [59] although other authors have disagreed with this correlation [20]. It is important to note that in the present work, that the estimated grain size of 76 to 315 nm was larger than the sizes reported by these two groups which on average was not larger than 12 nm [20,59]. Thus, factors which influence the Raman shift and intensity are the grain size range, the grain size of the oxide, along with the roughness.

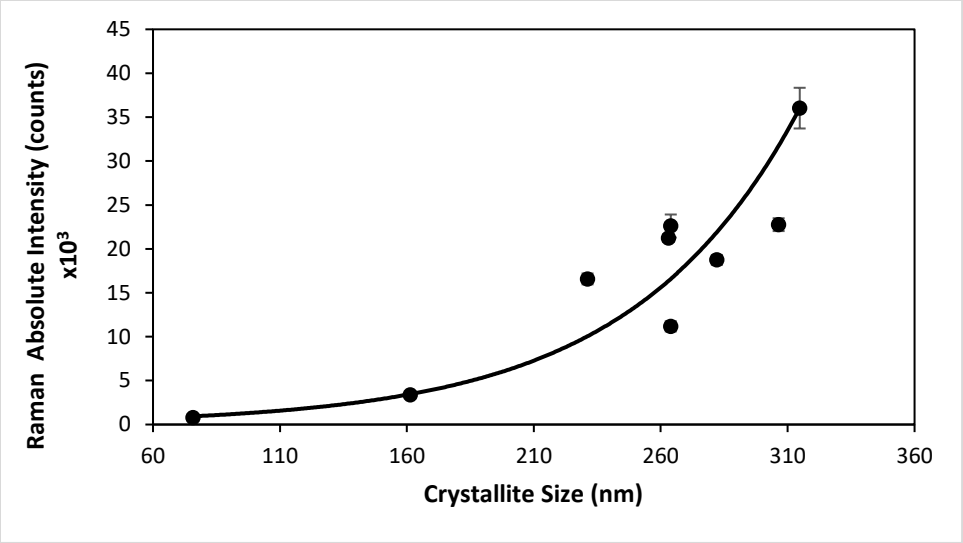

Figure 10: Plot of Raman absolute intensity against the estimated crystallite size of the treated samples.

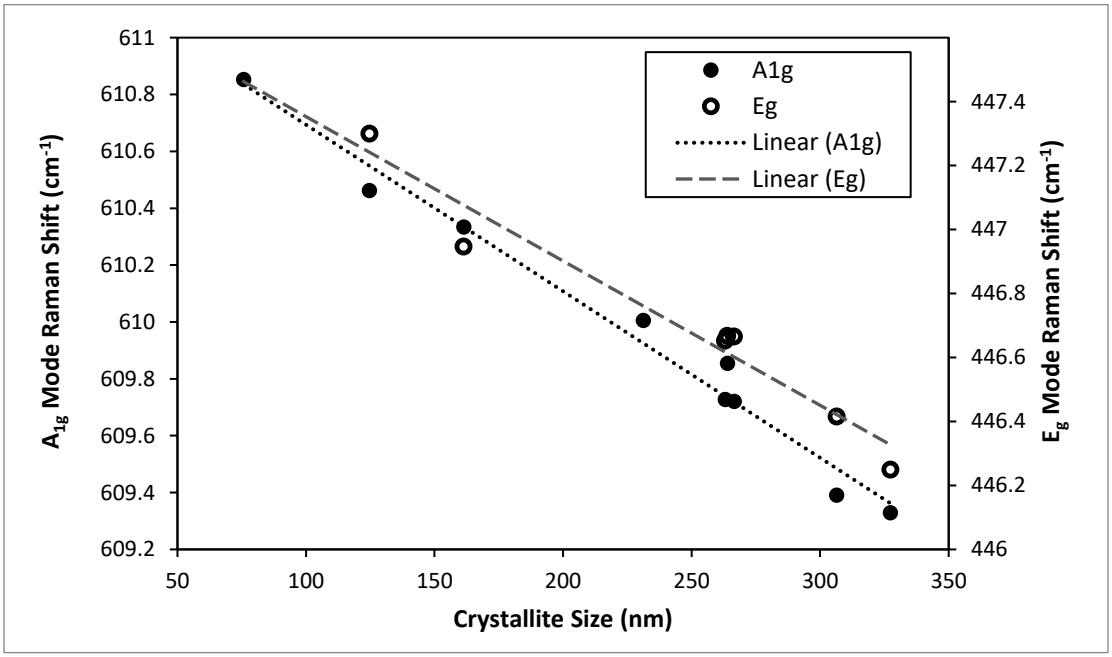

Figure 11: Correlation between the positions of the rutile A_{1g} (filled black circles) and E_g (open circles) peaks and TiO_2 crystallite size.

3.4 Influence of microwave processing conditions on the roughness parameters and Pore Structure of oxide layers

The evaluation of surface roughness is important in applications related to friction, contact deformation, heat and electric conduction, contact joints, positional accuracy [60] as well as surface enhanced scattering [61,62]. The average surface roughness (S_a) is the most commonly used roughness parameter and provides a very good overall height variation, although its lack of sensitivity to small changes in profile and wavelength information has been reported [60,63]. The skewness parameter S_{sk} is sensitive to occasional deep valleys or high peaks. A skewness value of zero implies a symmetrical height distribution, whereas positive skewness describes a surface with filled valleys or high peaks. A negative skewness represents a surface with lack of peaks. Kurtosis parameter S_{ku} describes the probability density sharpness of the profile and represents the peakedness degree of a surface height distribution. An S_{ku} value of < 3 implies that the surface has mostly few high peaks and low valleys while a value > 3 implies a surface with many high peaks and low valleys [60].

The influence of microwave plasma processing conditions on the commonly used 3D roughness parameters of the oxide layers are presented. The effect of input power on the amplitude (Average surface roughness S_a, Skewness S_{sk}; and Kurtosis S_{ku}) and hybrid (Root-Mean-Square Surface Slope S_{dq}) parameters is shown in Fig. 12. It can be observed that as the input power increased during processing, the average surface roughness amplitude (S_a) and hybrid (S_{dq}) parameters increased (Fig. 12 (A)). Similar trends were obtained for processing conditions of pressure and time except for the S_{dq} values obtained during treatment time which did not show any change. These results are presented in the supplementary material (Fig. S7). In order to understand the influence of microwave plasma input power on the oxide surface evolution, the values of S_{sk} and S_{ku} is presented for samples processed in the range of 0.9-2.1 kW at a pressure and time of 4.6 kpa and 10 minutes, respectively (Fig. 12 (B)). By considering the skewness parameter S_{sk}, it can be observed a change in morphology consistent with a transformation from a combination effect (where the surfaces were composed of a combination of small and large pores; and low and high peaks) found in the sample processed at 0.9 kW to one whose surfaces indicated positive skewness. The positive skewness indicates that the morphology of the samples processed in the range 1.5 – 2.1 kW consisted of mostly high peaks and large pore structure. The value of the kurtosis parameter S_{ku} were all above 3 for all samples treated in the range of 0.9 - 2.1 kW indicating that the oxide surfaces contained mostly high peaks and low valleys. Similar results were obtained for samples processed at 5 to 25 minutes using an input power and pressure of 1.2 kW and 4.6

kPa, respectively (see Figs. S8 & S9). For the samples treated using a pressure in the range of 1 - 5 kPa at 1.2 kW over a treatment period of 10 minutes; the skewness transitioned from a negative to positive value at a pressure range of 1 - 2 kPa. This gradually changed back to a negative skewness value with increasing treatment pressure indicating that the chamber pressure was the dominant factor influencing the growth rate of the oxide layer (Fig. 13). The kurtosis values indicate that the surface of the samples processed at low pressure (1 - 2 kPa) contained higher percentage of sharp peaks than the ones processed at higher pressures. Another useful indication is that low pressure treatments resulted in surfaces with a high morphological variation compared to the oxide surfaces obtained at higher pressure where a relatively homogeneous morphology was obtained (Fig. S10). The discussed effect of the morphological variation in the samples treated using various processing conditions can be observed on the level of intensity of the Raman spectra (Fig. 3) as the processing conditions are altered. This will be discussed further in subsequent sections.

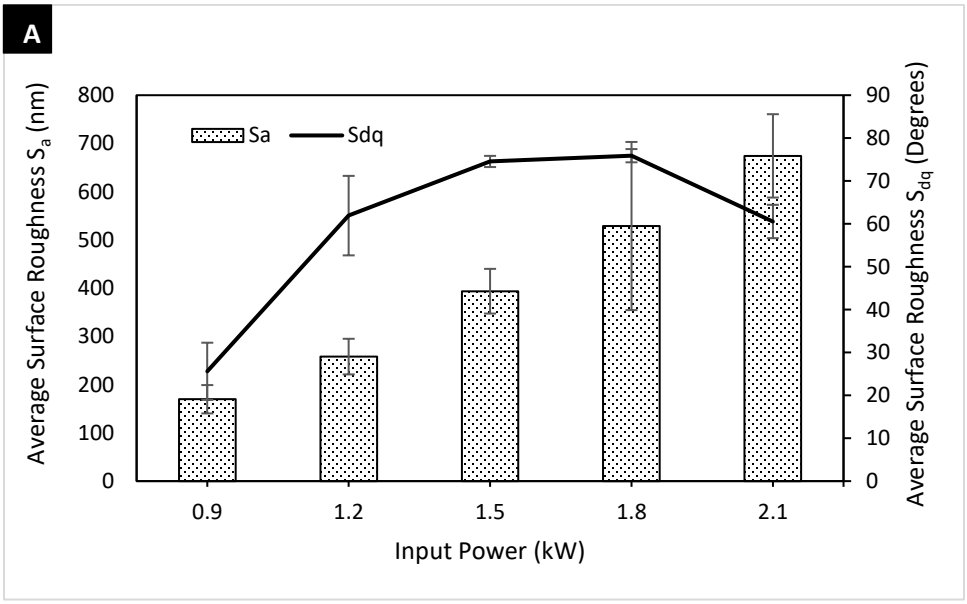

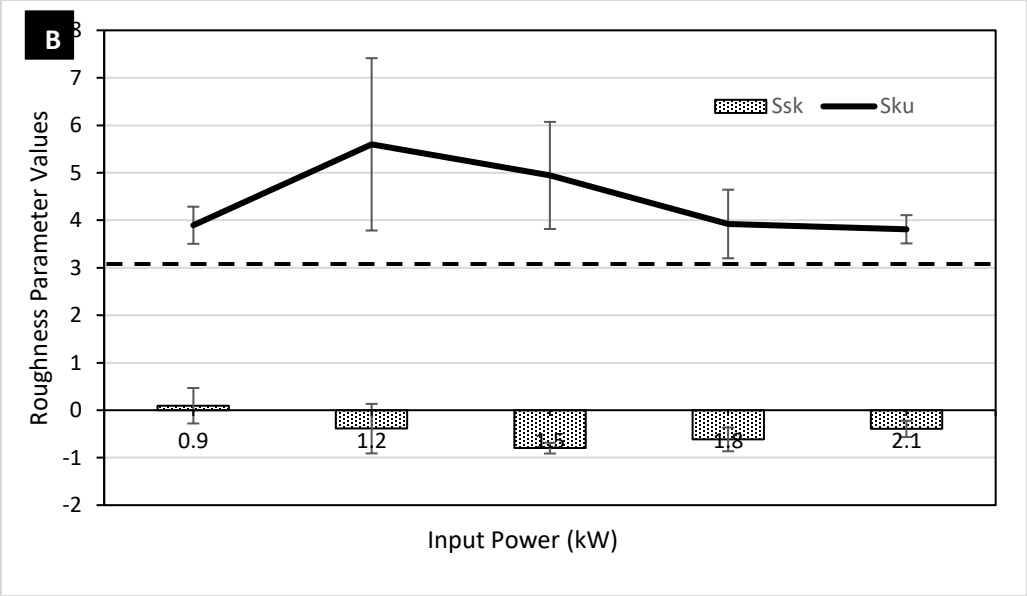

Figure 12: Effect of microwave plasma input power on the roughness parameters (S_a, S_{dq}, S_{sk} and S_{ku}) of the oxide layer.

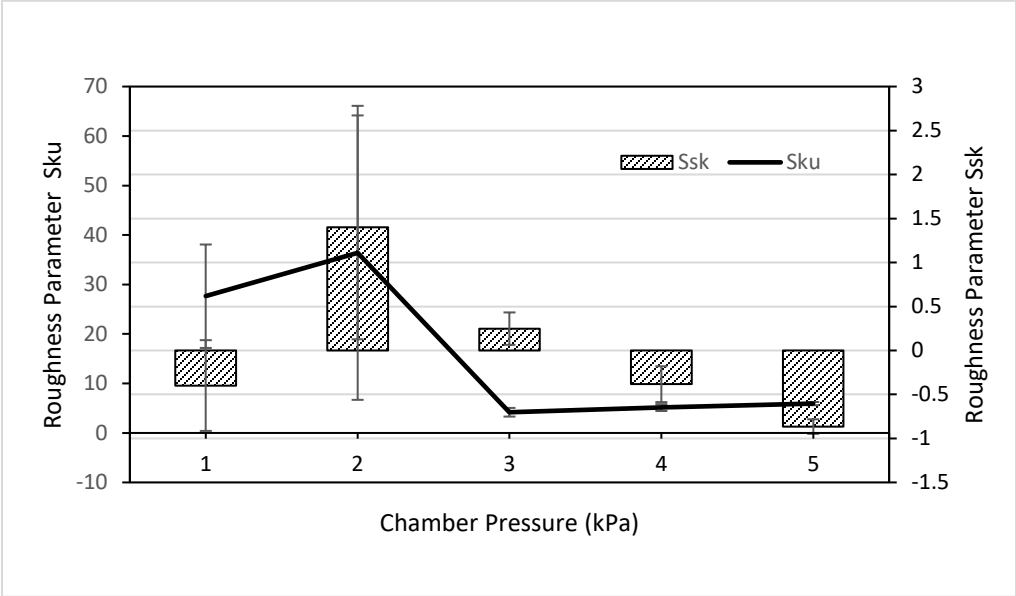

Figure 13: Influence of treatment pressure on the roughness parameters (S_{sk} & S_{ku}) of oxide layer samples processed in the range of 1 – 5 kPa.

3.5 Influence of Roughness Parameter (S_a) on Raman Intensity

It can be observed in Figs. 3 & 5 that the peak intensities and line width are clearly influenced by the microwave plasma process conditions. Also, the surface roughness parameters showed a correlation with the processing conditions as discussed in section 3.4. The dispersion of the measured intensity as a

function of the focusing point on the surface and the reproducibility of the measured values was considered by carrying out scans at five different regions on a sample (three measurements at each region) and then averaging the results. Thus, the change in intensity (as process conditions change) may be due to change in surface roughness and related open pore morphology of the oxide samples [61,62,64,65]. It has been reported that the physical structure of some surfaces can be related to the intensity of Raman scattering; and this phenomenon is currently applied in the detection of molecules by Surface Enhanced Raman Scattering (SERS) method [66–72]. The SERS enhancements generally depend on the features of the substrates, such as surface morphology, size, surface roughness and porosity [61]. In this study, the A_{1g} band was used to study the effect of average surface roughness (S_a) on the intensity of the Raman spectra obtained for the treated samples. The reason for the use of the average surface roughness (S_a) as the representative roughness parameter lies in the fact that it the most commonly used roughness parameter in literature and it is easily comprehensive. The dependence of the Raman peak intensity on the average surface roughness (S_a) is shown in Fig. 14. There is a clear correlation between the Raman peak intensity and the average surface roughness (S_a). A plot of Raman peak intensity (both absolute and baseline corrected intensities) against average surface roughness (S_a) of the 10 oxide samples investigated was found to be independent of treatment conditions (Fig. 14). It is unclear the mechanism(s) of the correlation observed between Raman intensity and roughness of the oxide layers, however, reports have shown that enhanced Raman scattering in semiconductor nanostructures may be attributed to contributions from a number of resonance effects, namely, surface plasmon, exciton, charge-transfer and molecular resonances [69,71,73].

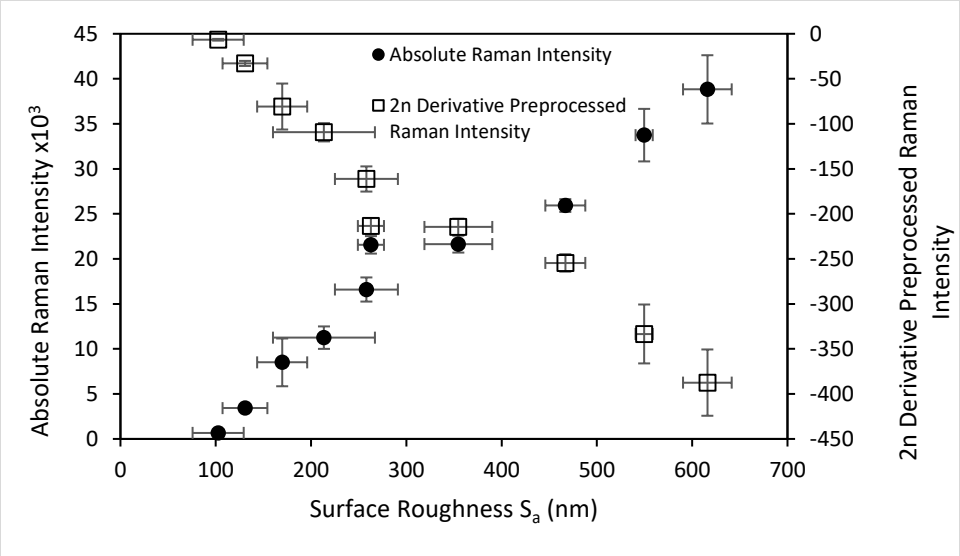

Figure 14: The relationship between average surface roughness (S_a) and Raman intensity of the A_{1g} band independent of microwave plasma treatment conditions.

In order to further investigate the correlation between average surface roughness and Raman absolute intensity, titanium samples were oxidized using input powers of 1.5 kW and 1.8 kW, with three samples evaluated at each power. Each test sample after being examined using Raman Spectroscopy, was ground to reduce its roughness and then re-examined. Samples grown at 1.5 kW did not indicate any significant change in Raman intensity when the average surface roughness was reduced by grinding. However, samples grown at 1.8 kW showed a 16% increase in Raman intensity when the average surface roughness of the samples was reduced. Examination of roughness parameters such as the amplitude (other than S_a), spatial, hybrid and functional parameters, which are related to the overall height, frequency, combination of height and frequency, and function application of surface features, respectively, revealed changes in the values of these parameters after grinding. Thus, the observed changes in the Raman intensity of oxide layers after grinding was influenced by the change in the S_a values as a function of other roughness parameters. This confirms the sensitivity of Raman spectra intensity to roughness of oxide layer prepared by a low-pressure microwave plasma. It must be stated, however, that the technique of manually grinding down the oxide surface did not produce a surface with reproducible roughness parameter values. Thus, the above stated effect of manual grinding is mostly qualitative.

3.6 Prediction of Surface Roughness from Raman Spectra using Multivariate Partial Least Squares Regression (PLSR)

3.6.1 Prediction of Surface Roughness from Point Raman Spectra

The Raman spectra intensity of the samples used in this study was correlated to their surface roughness (S_a) as discussed in section 3.5. This is supported by the Raman spectra of representative samples which clearly show that the intensity of the main peaks increased with increasing roughness (Fig. 15). The second derivative pretreated spectra are shown in Fig. S11. Clearly the baseline has been removed and the major peaks at the E_g and A_{1g} bands are visible as negative peaks in the second derivative spectra. In order to predict the roughness of the samples base on their Raman intensity, point spectra were taken at five regions (C, R1, R2, R3, & R5) on each sample which resulted in 50 data points. These were analysed and a PLS model built on half of the total number of 10 samples evaluated, then used to predict the roughness of the rest of the samples. As shown in Fig. 16, a two-latent variable model on raw data can predict roughness with a coefficient of determination (R^2) of approx. 0.87 when applied to the independent group of oxide test samples. This compares well with a single channel prediction using only the 608 cm^{-1} band (R^2 approx. 0.81). When the PLS model was constructed on second derivative spectra, the model performance was lower than for the models built on absolute Raman intensity, leading to a R^2 of 0.82 on the prediction set (Fig. S12). For this reason, subsequent model validation on the mapping data was carried out using the absolute Raman intensity [74]

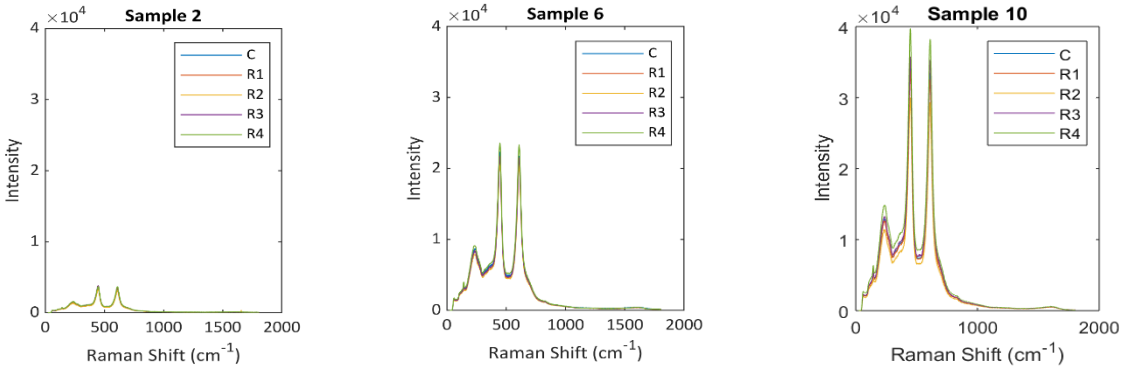

Figure 15: Raman spectra of typical samples showing correlation between intensity and surface roughness S_a.

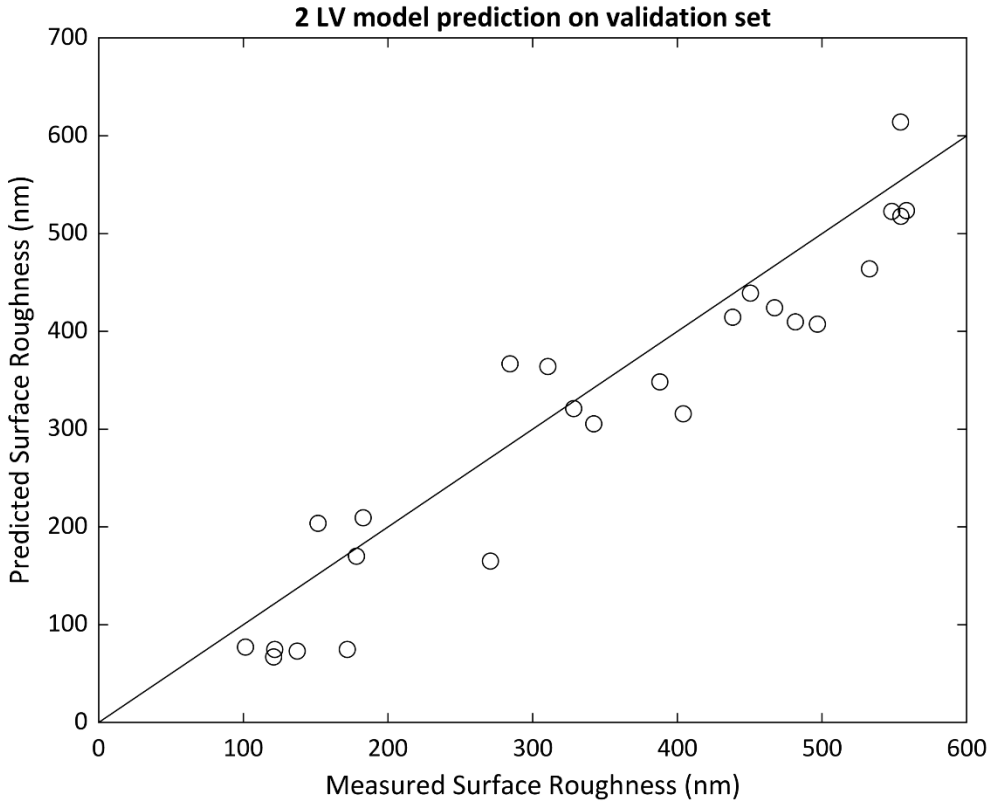

Figure 16: Multivariate PLS model to predict surface roughness.

3.6.2 *Prediction of Surface Roughness using Raman Mapping Data*

The PLSR model developed in the previous section was applied to the Raman map obtained over an area of 4x4 mm on a sample which was treated using an input power of 0.9 kW and at a pressure 4.6 kPa. The measured surface roughness of this sample based on the optical profilometry technique ranged from 142 – 217 nm, while the mean and standard deviation of roughness predicted from the Raman map were 179 and 29 respectively, indicating the accuracy of the PLSR model. The distribution of the predicted surface roughness values over the sampled area are shown in Fig. 17, where the prediction map and its corresponding histogram are visualised. The prediction map enables variation in the Roughness over the sample surface to be visualised. Overall, the distribution of Roughness values is symmetric, however, a small number of pixels were predicted to have considerably large Roughness values, i.e. 0.19% of pixels had a predicted Roughness > 300 nm. Examination of the corresponding spectra revealed spectral features consistent with fluorescence, which may have been due to the presence of small dust particles or other organic contamination on the sample surface.

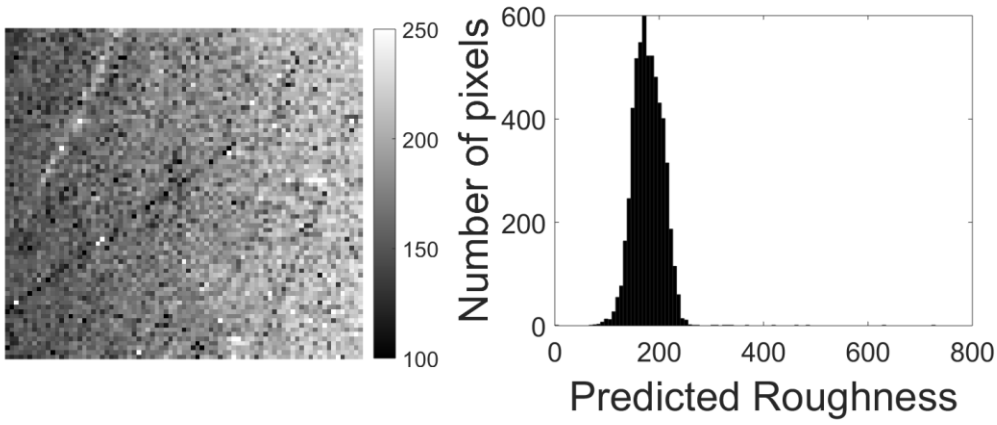

Figure 17: Prediction map enables variation in the Roughness over the sample surface to be visualised (left hand side) and histogram of prediction map (right hand side) obtained by applying PLSR model to Raman area map of the TiO_2 layer (area size 4x4 mm with 50 µm step size).

4. Conclusions

This study evaluated how the physical features of an oxide layer of titanium metal processed using various oxygen microwave plasma conditions (input power, treatment time and pressure) influenced the linewidth, peak position and intensity of the Raman bands (E_g and A_{1g}) obtained. It was concluded that the intensity of the representative band (A_{1g}) of the TiO_2 was influenced by the average surface roughness (S_a) irrespective of processing condition and the oxide crystallite size. Based on the review of the effect of the physical features of the oxide layer processed using various microwave processing conditions such as input power, chamber pressure and time it was concluded that:

- The Titanium dioxide obtained using the microwave plasma treatment was mostly rutile.

- The presence of a low concentration of Ti_2O, Ti_3O_5 and some members of the homologous series (Ti_nO_{2n-1}) was also observed in the oxide structure.

- The processing conditions influenced the concentration of oxygen in the oxide layers.

- A 1-fold increase and decrease in the linewidth of E_g and A_{1g} bands was observed, respectively, with increasing input power. For samples processed in the range of 5 to 25 minutes, both E_g and A_{1g} band linewidths decreased by 1-fold. In this case of pressure, the linewidths decreased and increased for E_g and A_{1g} bands, respectively, as the pressure changed from 1 kPa to 2 kPa.

- Analysis of the peak positions of E_g and A_{1g} modes indicated that the effects of input power and chamber pressure was to induce a shift towards the lower frequency with increasing input power and pressure (1-2 kPa). However, as the pressure increased to the range of 3 to 5 kPa, there was no significant redshift observed. Samples processed for 5 to 15 minutes induced a slight shift towards the higher frequency for the E_g band; whereas for the A_{1g} band, there was not significant effect on the Raman peak positions. For samples processed using more than 15 minutes, both the E_g and A_{1g} bands exhibited a redshift.

- The crystallite size influenced the intensity and the band position of the Raman spectra.

- There was a correlation between the average surface roughness (S_a) of the oxides and the Raman intensity observed. The correlation was found to be largely independent of the microwave plasma processing conditions used to obtain the oxide.

- The relationship between surface roughness and Raman scattering was further explored by the development of Partial Least Square Regression model to predict surface roughness. The resulting model was found to facilitate accurate prediction of roughness, with a coefficient of determination (R^2) of approx. 0.87, when applied to the independent test set. The developed model, when applied to a Raman map of the surface of a sample, provided information on the spatial distribution of roughness over the sample surface while also indicating the accuracy of the model.

Acknowledgments

The authors would like to acknowledge the support of SFI funded I-Form Advanced Manufacturing Research Centre 16/RC/3872. The second and third author acknowledge funding from the EU FP7 under the European Research Council Starting Grant programme (ERC-SG-335508).

References

[1] Hardcastle FD, Wachs IE. Determination of vanadium-oxygen bond distances and bond orders by Raman spectroscopy. J Phys Chem 1991;95:5031–41. doi:10.1021/j100166a025.

[2] Liu X, Chu PK, Ding C. Surface modification of titanium, titanium alloys, and related materials for biomedical applications. Mater Sci Eng R Reports 2004;47:49–121. doi:10.1016/J.MSER.2004.11.001.

[3] FUJISHIMA A, HONDA K. Electrochemical Photolysis of Water at a Semiconductor Electrode. Nature 1972;238:37–8. doi:10.1038/238037a0.

[4] Hanaor DAH, Sorrell CC. Sand Supported Mixed-Phase TiO_2 Photocatalysts for Water Decontamination Applications. Adv Eng Mater 2014;16:248–54. doi:10.1002/adem.201300259.

[5] Darius Kuciauskas, Michael S. Freund, Harry B. Gray *, Jay R. Winkler * and, Lewis* NS. Electron Transfer Dynamics in Nanocrystalline Titanium Dioxide Solar Cells Sensitized with Ruthenium or Osmium Polypyridyl Complexes 2000. doi:10.1021/JP002545L.

[6] Deo G, Turek AM, Wachs IE, Machej T, Haber J, Das N, et al. Physical and chemical characterization of surface vanadium oxide supported on titania: influence of the titania phase (anatase, rutile, brookite and B). Appl Catal A Gen 1992;91:27–42. doi:10.1016/0926-860X(92)85176-C.

[7] Porto SPS, Fleury PA, Damen TC. Raman Spectra of Ti O 2 , Mg F 2 , Zn F 2 , Fe F 2 , and Mn F 2. Phys Rev 1967;154:522–6. doi:10.1103/PhysRev.154.522.

[8] Lukačević I, Gupta SK, Jha PK, Kirin D. Lattice dynamics and Raman spectrum of rutile TiO2: The role of soft phonon modes in pressure induced phase transition. Mater Chem Phys 2012;137:282–9. doi:10.1016/J.MATCHEMPHYS.2012.09.022.

[9] Ma HL, Yang JY, Dai Y, Zhang YB, Lu B, Ma GH. Raman study of phase transformation of TiO2 rutile single crystal irradiated by infrared femtosecond laser. Appl Surf Sci 2007;253:7497–500. doi:10.1016/J.APSUSC.2007.03.047.

[10] Arsov LD, Kormann C, Plieth W. Electrochemical synthesis and in situ Raman spectroscopy of thin films of titanium dioxide. J Raman Spectrosc 1991;22:573–5. doi:10.1002/jrs.1250221006.

[11] Ohsaka T, Izumi F, Fujiki Y. Raman spectrum of anatase, TiO2. J Raman Spectrosc 1978;7:321–4.

doi:10.1002/jrs.1250070606.

[12] Tompsett GA, Bowmaker GA, Cooney RP, Metson JB, Rodgers KA, Seakins JM. The Raman spectrum of brookite, TiO2 (Pbca, Z = 8). J Raman Spectrosc 1995;26:57–62. doi:10.1002/jrs.1250260110.

[13] Sekiya T, Ohta S, Kamei S, Hanakawa M, Kurita S. Raman spectroscopy and phase transition of anatase TiO2 under high pressure. J Phys Chem Solids 2001;62:717–21. doi:10.1016/S0022-3697(00)00229-8.

[14] Yan J, Wu G, Guan N, Li L, Li Z, Cao X. Understanding the effect of surface/bulk defects on the photocatalytic activity of TiO2: anatase versus rutile. Phys Chem Chem Phys 2013;15:10978. doi:10.1039/c3cp50927c.

[15] Lan T, Tang X, Fultz B. Phonon anharmonicity of rutile TiO 2 studied by Raman spectrometry and molecular dynamics simulations. Phys Rev B 2012;85:094305. doi:10.1103/PhysRevB.85.094305.

[16] Aita CR. Raman scattering by thin film nanomosaic rutile TiO2. Appl Phys Lett 2007;90:213112. doi:10.1063/1.2742914.

[17] Swamy V, Muddle BC, Dai Q. Size-dependent modifications of the Raman spectrum of rutile TiO2. Appl Phys Lett 2006;89:163118. doi:10.1063/1.2364123.

[18] Zhang Y, Harris CX, Wallenmeyer P, Murowchick J, Chen X. Asymmetric Lattice Vibrational Characteristics of Rutile TiO_2 as Revealed by Laser Power Dependent Raman Spectroscopy. J Phys Chem C 2013;117:24015–22. doi:10.1021/jp406948e.

[19] Jiang X, Zhang Y, Jiang J, Rong Y, Wang Y, Wu Y, et al. Characterization of Oxygen Vacancy Associates within Hydrogenated TiO_2 : A Positron Annihilation Study. J Phys Chem C 2012;116:22619–24. doi:10.1021/jp307573c.

[20] Mazza T, Barborini E, Piseri P, Milani P, Cattaneo D, Li Bassi A, et al. Raman spectroscopy characterization of Ti O 2 rutile nanocrystals. Phys Rev B 2007;75:045416. doi:10.1103/PhysRevB.75.045416.

[21] Li Bassi A, Cattaneo D, Russo V, Bottani CE, Barborini E, Mazza T, et al. Raman spectroscopy characterization of titania nanoparticles produced by flame pyrolysis: The influence of size and

stoichiometry. J Appl Phys 2005;98:074305. doi:10.1063/1.2061894.

[22] Tian F, Zhang Y, Zhang J, Pan C. Raman Spectroscopy: A New Approach to Measure the Percentage of Anatase TiO $_2$ Exposed (001) Facets. J Phys Chem C 2012;116:7515–9. doi:10.1021/jp301256h.

[23] Jing Zhang, Meijun Li, Zhaochi Feng, Jun Chen and, Li* C. UV Raman Spectroscopic Study on TiO2. I. Phase Transformation at the Surface and in the Bulk 2005. doi:10.1021/JP0552473.

[24] Hardcastle FD. Raman Spectroscopy of Titania (TiO 2) Nanotubular Water-Splitting Catalysts. vol. 65. 2011.

[25] Lu G, Bernasek SL, Schwartz J. Oxidation of a polycrystalline titanium surface by oxygen and water. Surf Sci 2000;458:80–90. doi:10.1016/S0039-6028(00)00420-9.

[26] Pérez del Pino A, Serra P, Morenza J. Oxidation of titanium through Nd:YAG laser irradiation. Appl Surf Sci 2002;197–198:887–90. doi:10.1016/S0169-4332(02)00447-6.

[27] Gemelli E, Camargo NHA. Oxidation kinetics of commercially pure titanium. Matéria 2007;12:525–31. doi:10.1590/S1517-70762007000300014.

[28] Li L-H, Kong Y-M, Kim H-W, Kim Y-W, Kim H-E, Heo S-J, et al. Improved biological performance of Ti implants due to surface modification by micro-arc oxidation. Biomaterials 2004;25:2867–75. doi:10.1016/J.BIOMATERIALS.2003.09.048.

[29] Diefenbeck M, Mückley T, Schrader C, Schmidt J, Zankovych S, Bossert J, et al. The effect of plasma chemical oxidation of titanium alloy on bone-implant contact in rats. Biomaterials 2011;32:8041–7. doi:10.1016/J.BIOMATERIALS.2011.07.046.

[30] Kofstad P, Hauffe K, Kjollesdal H, Reilly JJ, Wiswall RH. Investigation on the Oxidation Mechanism of Titanium. Acta Chem Scand 1958;12:239–66. doi:10.3891/acta.chem.scand.12-0239.

[31] Orii Y, Masumoto H, Honda Y, Anada T, Goto T, Sasaki K, et al. Enhancement of octacalcium phosphate deposition on a titanium surface activated by electron cyclotron resonance plasma oxidation. J Biomed Mater Res Part B Appl Biomater 2010;93B:476–83. doi:10.1002/jbm.b.31605.

[32] Zwilling V, Aucouturier M, Darque-Ceretti E. Anodic oxidation of titanium and TA6V alloy in chromic media. An electrochemical approach. Electrochim Acta 1999;45:921–9. doi:10.1016/S0013-4686(99)00283-2.

[33] Zwilling V, Darque-Ceretti E, Boutry-Forveille A, David D, Perrin MY, Aucouturier M. Structure and physicochemistry of anodic oxide films on titanium and TA6V alloy. Surf Interface Anal 1999;27:629–37. doi:10.1002/(SICI)1096-9918(199907)27:7<629::AID-SIA551>3.0.CO;2-0.

[34] Aronsson B-O, Lausmaa J, Kasemo B. Glow discharge plasma treatment for surface cleaning and modification of metallic biomaterials. J Biomed Mater Res 1997;35:49–73. doi:10.1002/(SICI)1097-4636(199704)35:1<49::AID-JBM6>3.0.CO;2-M.

[35] Kakizaka S, Sakamoto T, Matsuura H, Akatsuka H. Titanium Oxidation by Microwave Discharge Oxygen Plasma and Relationship with Plasma Parameters. J Adv Oxid Technol 2007;10:253–9. doi:10.1515/jaots-2007-0205.

[36] Ekoi EJ, Stallard C, Reid I, Dowling DP. Tailoring oxide-layer formation on titanium substrates using microwave plasma treatments. Surf Coatings Technol 2017;325. doi:10.1016/j.surfcoat.2017.06.046.

[37] Ekoi E, Awais M, Dowling D. Microwave Plasmas as a Processing Tool for Tailoring the Surface Properties of Ceramic Coatings. In: Basheer Al-Naib U, editor. Recent Adv. Porous Ceram., IntechOpen; 2018. doi:DOI: 10.5772/intechopen.71686.

[38] Patterson AL. The Scherrer Formula for X-Ray Particle Size Determination. Phys Rev 1939;56:978–82. doi:10.1103/PhysRev.56.978.

[39] Langford JI, Wilson AJC. Scherrer after sixty years: A survey and some new results in the determination of crystallite size. J Appl Crystallogr 1978;11:102–13. doi:10.1107/S0021889878012844.

[40] Gowen AA, Downey G, Esquerre C, O'Donnell CP. Preventing over-fitting in PLS calibration models of near-infrared (NIR) spectroscopy data using regression coefficients. J Chemom 2011;25:375–81. doi:10.1002/cem.1349.

[41] Lawless KR. The oxidation of metals. Reports Prog Phys 1974;37:231–316. doi:10.1088/0034-4885/37/2/002.

[42] Miles JL, Smith PH. The Formation of Metal Oxide Films Using Gaseous and Solid Electrolytes. J Electrochem Soc 1963;110:1240. doi:10.1149/1.2425633.

[43] Schroen W. Physics of Preparation of Josephson Barriers. J Appl Phys 1968;39:2671–8.

doi:10.1063/1.1656651.

[44] Hayashi Y, Drawl W, Messier R. Temperature Dependence of Nucleation Density of Chemical Vapor Deposition Diamond. Jpn J Appl Phys 1992;31:L193–6. doi:10.1143/JJAP.31.L193.

[45] Tang CJ, Neves AJ, Fernandes AJS. Influence of nucleation density on film quality, growth rate and morphology of thick CVD diamond films. Diam Relat Mater 2003;12:1488–94. doi:10.1016/S0925-9635(03)00179-1.

[46] Balachandran U, Eror NG. Raman spectra of titanium dioxide. J Solid State Chem 1982;42:276–82. doi:10.1016/0022-4596(82)90006-8.

[47] Yang M, Huang D, Hao P, Zhang F, Hou X, Wang X. Study of the Raman peak shift and the linewidth of light-emitting porous silicon. J Appl Phys 1994;75:651–3. doi:10.1063/1.355808.

[48] Richter H, Wang ZP, Ley L. The one phonon Raman spectrum in microcrystalline silicon. Solid State Commun 1981;39:625–9. doi:10.1016/0038-1098(81)90337-9.

[49] Campbell IH, Fauchet PM. The effects of microcrystal size and shape on the one phonon Raman spectra of crystalline semiconductors. Solid State Commun 1986;58:739–41. doi:10.1016/0038-1098(86)90513-2.

[50] Smith JR, Walsh FC, Clarke RL. Electrodes based on Magnéli phase titanium oxides: the properties and applications of Ebonex® materials. J Appl Electrochem 1998;28:1021–33. doi:10.1023/A:1003469427858.

[51] Liborio L, Mallia G, Harrison N. Electronic structure of the Ti_4O_7 Magnéli phase. Phys Rev B 2009;79:245133. doi:10.1103/PhysRevB.79.245133.

[52] Liborio L, Harrison N. Thermodynamics of oxygen defective Magnéli phases in rutile: A first-principles study. Phys Rev B 2008;77:104104. doi:10.1103/PhysRevB.77.104104.

[53] Anderson JS, Tilley RJD. Crystallographic shear in oxygen-deficient rutile: An electron microscope study. J Solid State Chem 1970;2:472–82. doi:10.1016/0022-4596(70)90106-4.

[54] Cho E, Han S, Ahn H-S, Lee K-R, Kim SK, Hwang CS. First-principles study of point defects in rutile TiO_{2-x}. Phys Rev B 2006;73:193202. doi:10.1103/PhysRevB.73.193202.

[55] Leng Y., Huang N, Yang P, Chen J., Sun H, Wang J, et al. Influence of oxygen pressure on the

properties and biocompatibility of titanium oxide fabricated by metal plasma ion implantation and deposition. Thin Solid Films 2002;420–421:408–13. doi:10.1016/S0040-6090(02)00814-3.

[56] Etacheri V, Seery MK, Hinder SJ, Pillai SC. Oxygen Rich Titania: A Dopant Free, High Temperature Stable, and Visible-Light Active Anatase Photocatalyst. Adv Funct Mater 2011;21:3744–52. doi:10.1002/adfm.201100301.

[57] She H, Zhou H, Li L, Wang L, Huang J, Wang Q. Nickel-Doped Excess Oxygen Defect Titanium Dioxide for Efficient Selective Photocatalytic Oxidation of Benzyl Alcohol. ACS Sustain Chem Eng 2018;6:11939–48. doi:10.1021/acssuschemeng.8b02217.

[58] Cabrera N, Mott NF. Theory of the oxidation of metals. Reports Prog Phys 1949;12:163–84. doi:10.1088/0034-4885/12/1/308.

[59] Parker JC, Siegel RW. Calibration of the Raman spectrum to the oxygen stoichiometry of nanophase TiO_2. Appl Phys Lett 1990;57:943–5. doi:10.1063/1.104274.

[60] Gadelmawla ES, Koura MM, Maksoud TMA, Elewa IM, Soliman HH. Roughness parameters. J Mater Process Technol 2002;123:133–45. doi:10.1016/S0924-0136(02)00060-2.

[61] Qian LH, Yan XQ, Fujita T, Inoue A, Chen MW. Surface enhanced Raman scattering of nanoporous gold: Smaller pore sizes stronger enhancements. Appl Phys Lett 2007;90:153120. doi:10.1063/1.2722199.

[62] Macias G, Alba M, Marsal LF, Mihi A. Surface roughness boosts the SERS performance of imprinted plasmonic architectures. J Mater Chem C 2016;4:3970–5. doi:10.1039/C5TC02779A.

[63] Sedlaček M, Podgornik B, Vižintin J. Correlation between standard roughness parameters skewness and kurtosis and tribological behaviour of contact surfaces. Tribol Int 2012;48:102–12. doi:10.1016/J.TRIBOINT.2011.11.008.

[64] Hildebrandt P, Stockburger M. Surface-enhanced resonance Raman spectroscopy of Rhodamine 6G adsorbed on colloidal silver. J Phys Chem 1984;88:5935–44. doi:10.1021/j150668a038.

[65] Kreibig U, Genzel L. Optical absorption of small metallic particles. Surf Sci 1985;156:678–700. doi:10.1016/0039-6028(85)90239-0.

[66] Nie S, Emory SR. Probing Single Molecules and Single Nanoparticles by Surface-Enhanced Raman Scattering. Science 1997;275:1102–6. doi:10.1126/SCIENCE.275.5303.1102.

[67] Xu H, Bjerneld EJ, Käll M, Börjesson L. Spectroscopy of Single Hemoglobin Molecules by Surface Enhanced Raman Scattering. Phys Rev Lett 1999;83:4357–60. doi:10.1103/PhysRevLett.83.4357.

[68] Kneipp K, Wang Y, Kneipp H, Perelman LT, Itzkan I, Dasari RR, et al. Single Molecule Detection Using Surface-Enhanced Raman Scattering (SERS). Phys Rev Lett 1997;78:1667–70. doi:10.1103/PhysRevLett.78.1667.

[69] Milekhin AG, Yeryukov NA, Sveshnikova LL, Duda TA, Kosolobov SS, Latyshev A V., et al. Raman Scattering for Probing Semiconductor Nanocrystal Arrays with a Low Areal Density. J Phys Chem C 2012;116:17164–8. doi:10.1021/jp210720v.

[70] Milekhin AG, Sveshnikova LL, Duda TA, Yeryukov NA, Rodyakina EE, Gutakovskii AK, et al. Surface-enhanced Raman spectroscopy of semiconductor nanostructures. Phys E Low-Dimensional Syst Nanostructures 2016;75:210–22. doi:10.1016/J.PHYSE.2015.09.013.

[71] Xue X, Ji W, Mao Z, Mao H, Wang Y, Wang X, et al. Raman Investigation of Nanosized TiO_2 : Effect of Crystallite Size and Quantum Confinement. J Phys Chem C 2012;116:8792–7. doi:10.1021/jp2122196.

[72] Bontempi N, Carletti L, De Angelis C, Alessandri I. Plasmon-free SERS detection of environmental CO_2 on TiO_2 surfaces. Nanoscale 2016;8:3226–31. doi:10.1039/C5NR08380J.

[73] Lombardi JR, Birke RL. Theory of Surface-Enhanced Raman Scattering in Semiconductors. J Phys Chem C 2014;118:11120–30. doi:10.1021/jp5020675.

[74] Colomban P, Slodczyk A. Raman intensity: An important tool to study the structure and phase transitions of amorphous/crystalline materials. Opt Mater (Amst) 2009;31:1759–63. doi:10.1016/J.OPTMAT.2008.12.030.

Supplementary Data

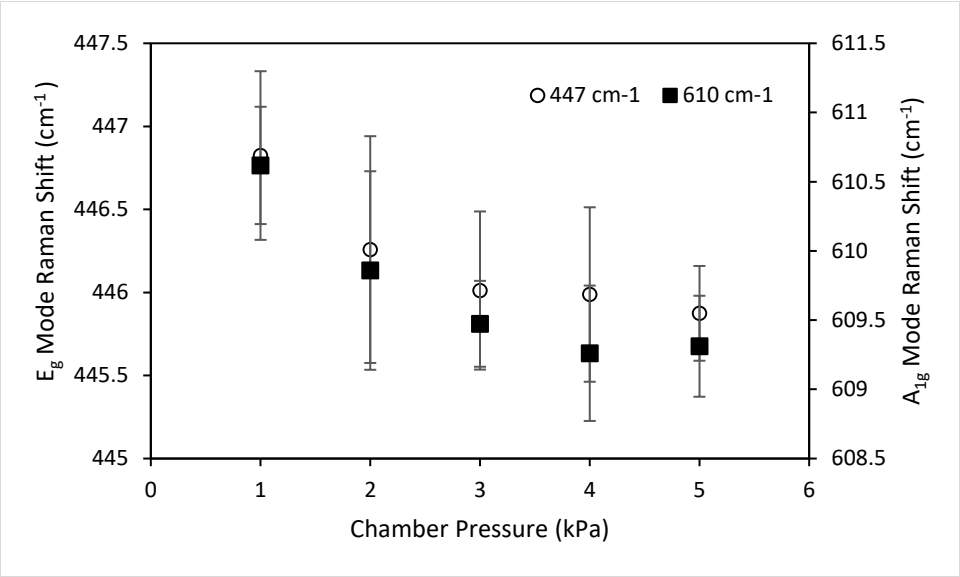

S1: Effect of pressure on the peak position for the E_g (447 cm^{-1}) and A_{1g} (610 cm^{-1}) Raman bands.

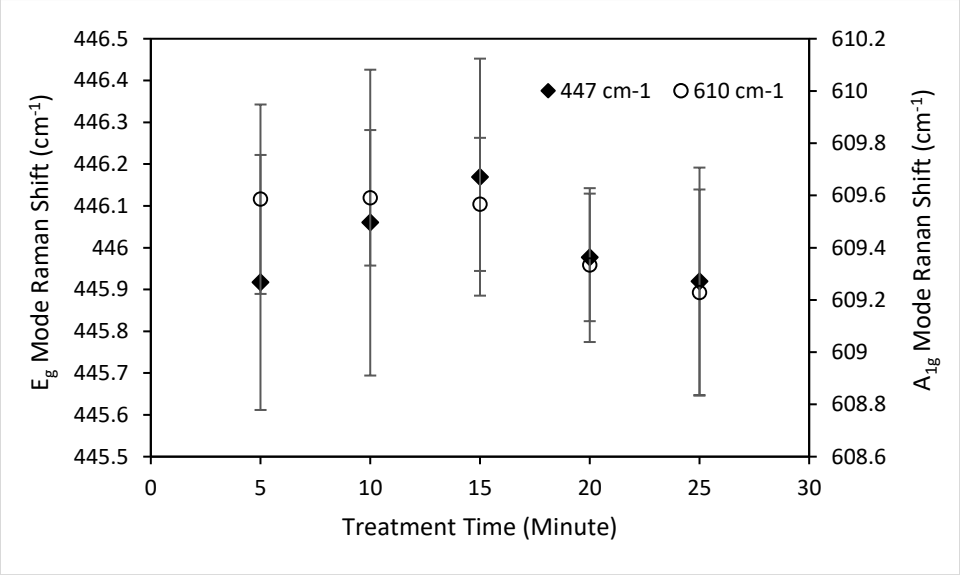

S2: Effect of treatment time on the peak position for the E_g (447 cm^{-1}) and A_{1g} (610 cm^{-1}) Raman bands.

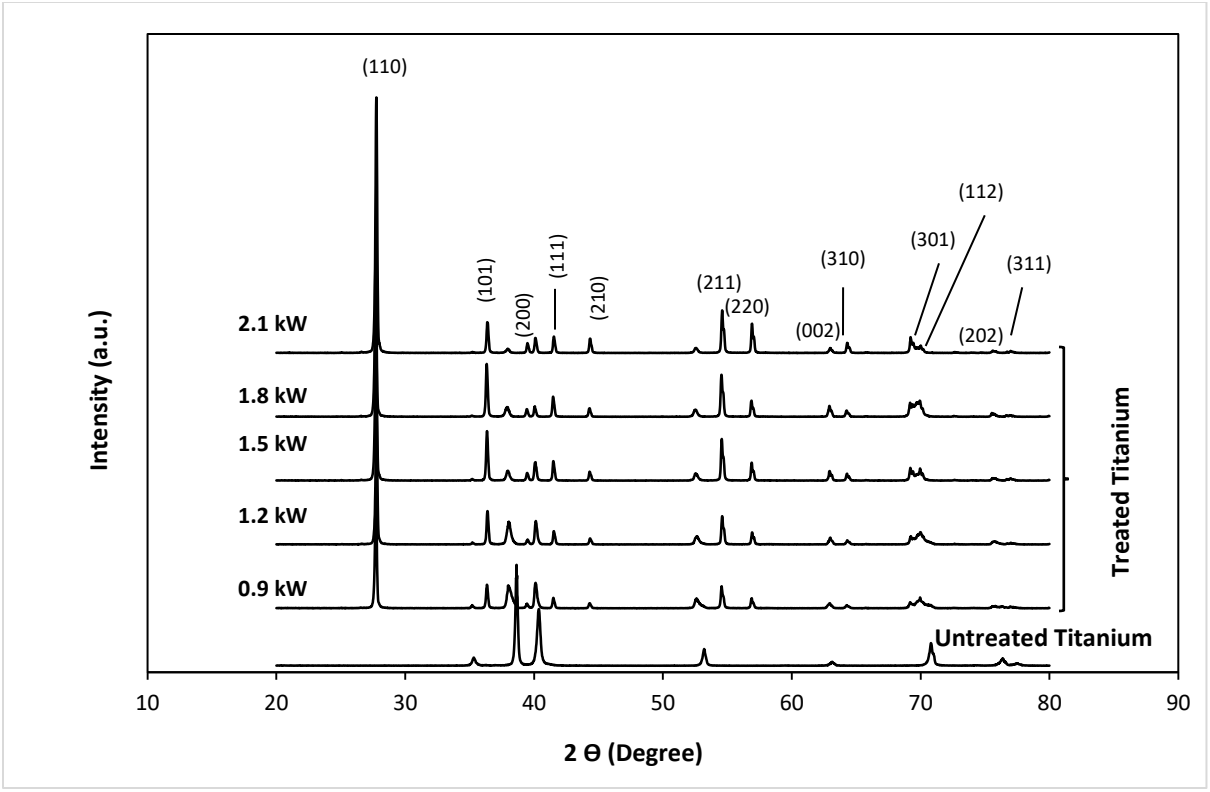

S3: XRD diffraction patterns obtained for untreated and plasma oxidised titanium using microwave plasma input power of 0.9 kW – 2.1 kW. The peaks indicate a Rutile TiO_2 was the dominant phase.

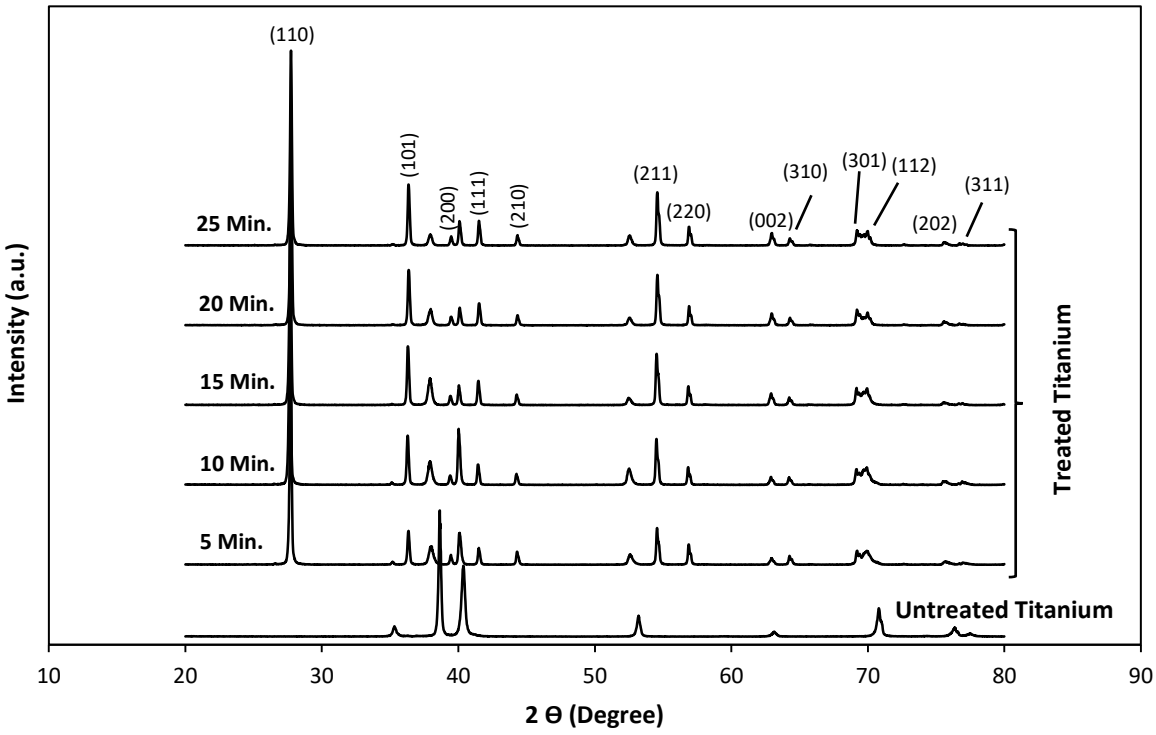

S4: XRD diffraction patterns obtained for untreated and plasma oxidised titanium using microwave plasma treatment time of 1 – 5 minutes. The peaks indicate a Rutile TiO_2 was the dominant phase.

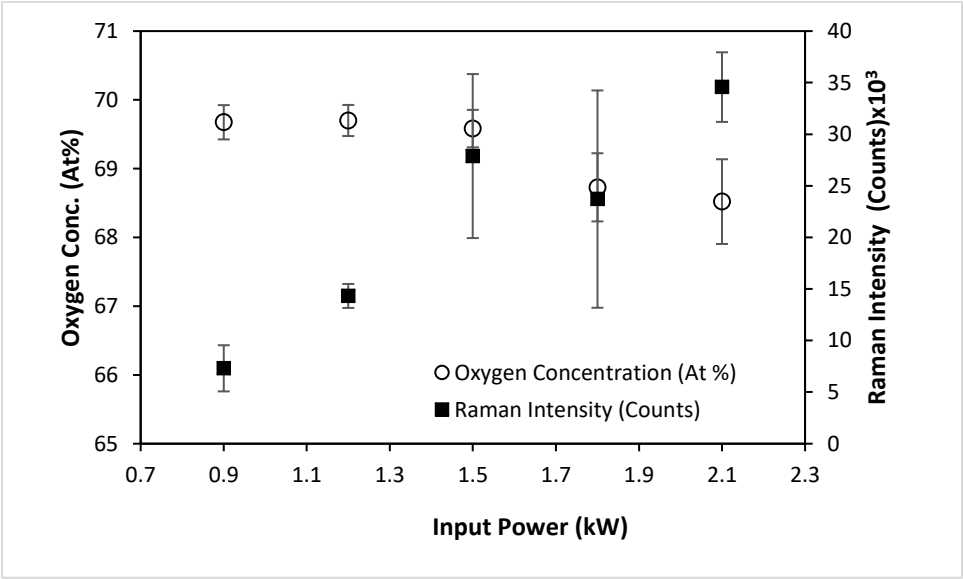

S5: Effect of input power on the oxygen concentration (At % weight) and the intensity of the A_{1g} Raman band.

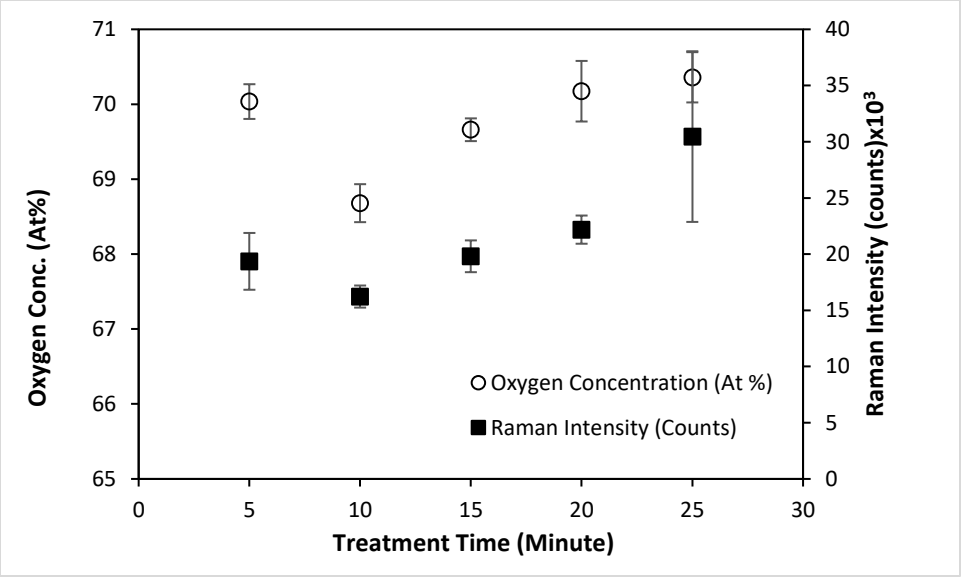

S6: Effect of treatment time on the oxygen concentration (At % weight) and the intensity of the A_{1g} Raman band.

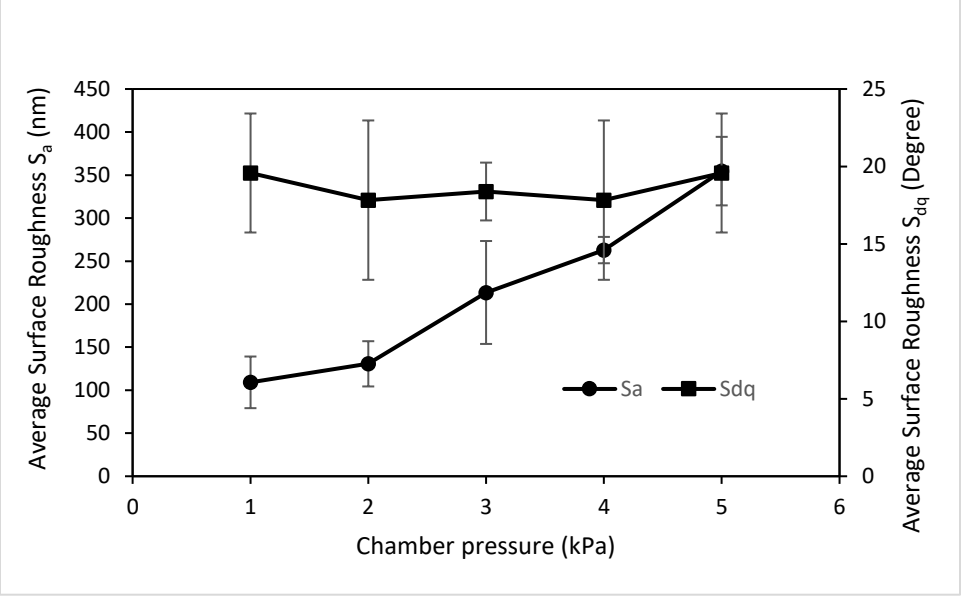

S7: Influence of chamber pressure on the roughness parameters S_a and S_{dq}.

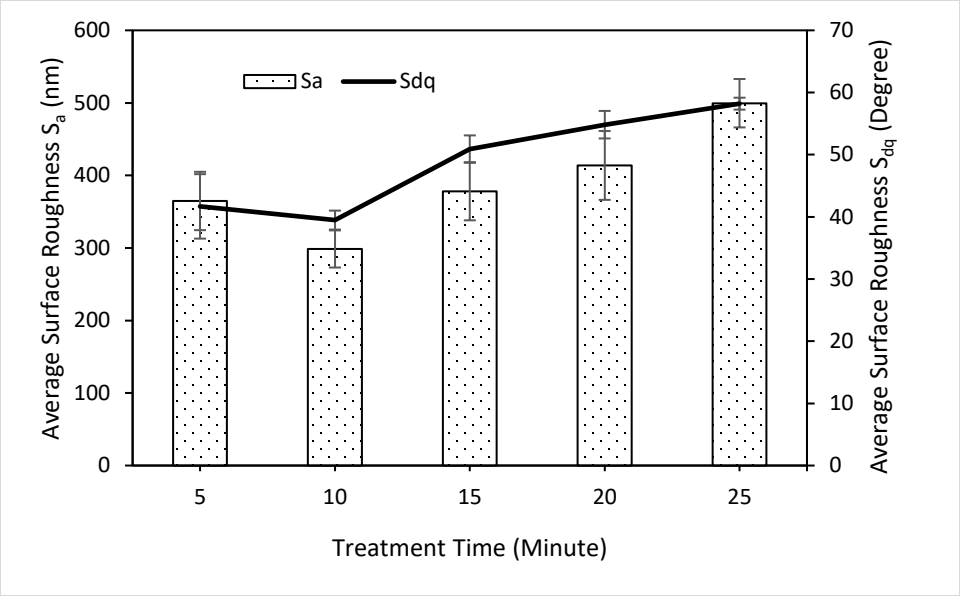

S8: Influence of treatment time on the roughness parameters S_a and S_{dq}.

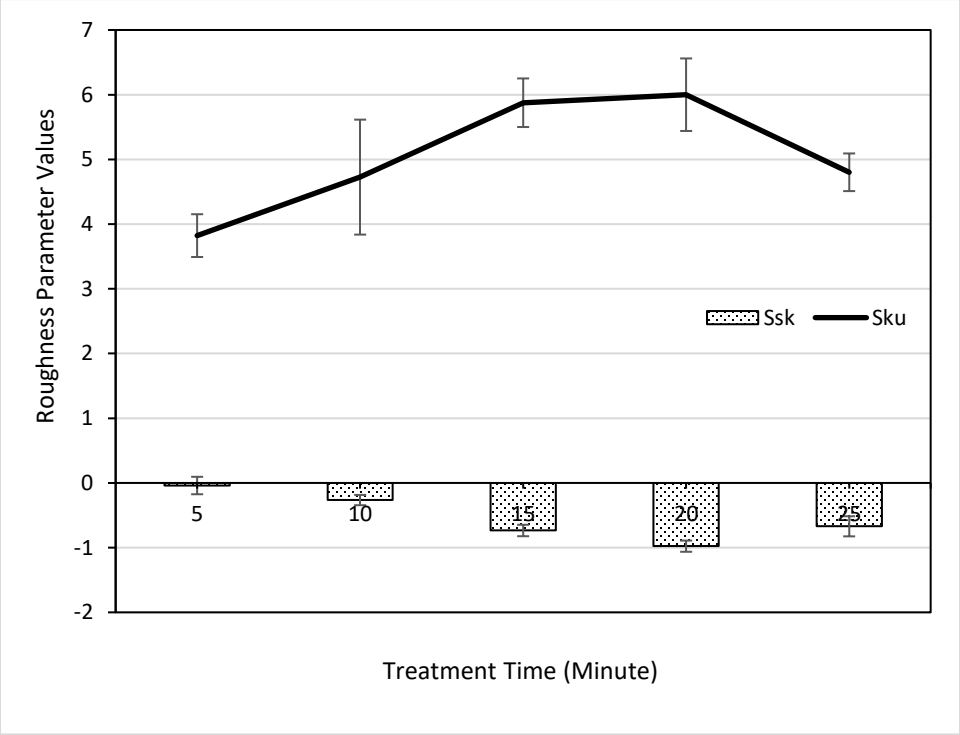

S9: Influence of treatment time on the roughness parameters S_{sk} and S_{ku}.

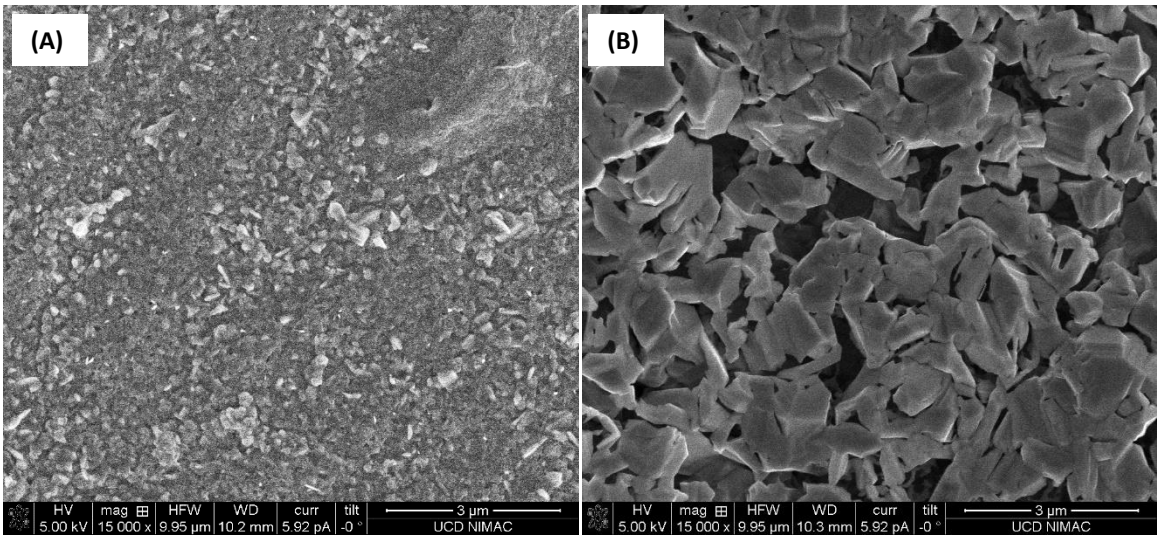

S10: Morphology of oxide layer grown using pressure of: (A) – 1 kPa & (B) – 5 kPa. Note that an input power and treatment time of 1.2 kW and 10 minutes, respectively, were used during processing.

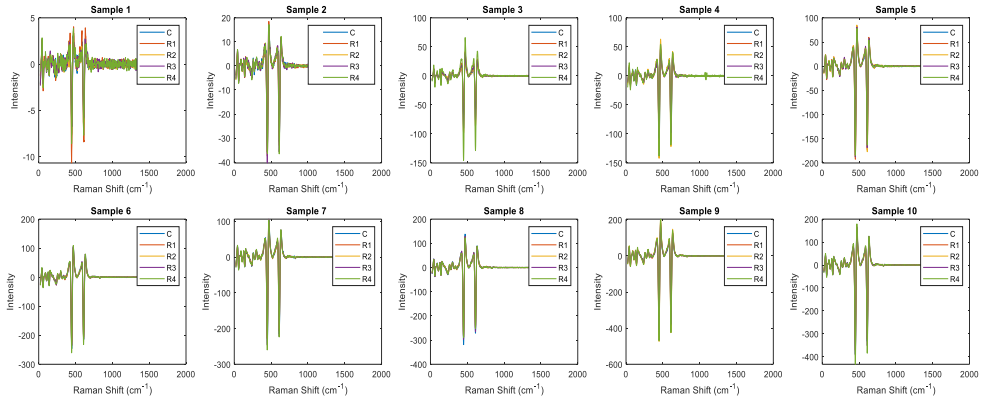

S11: Raman spectra of samples showing correlation between intensity (second derivative Savitsky Golay pretreatment) and surface roughness S_a.

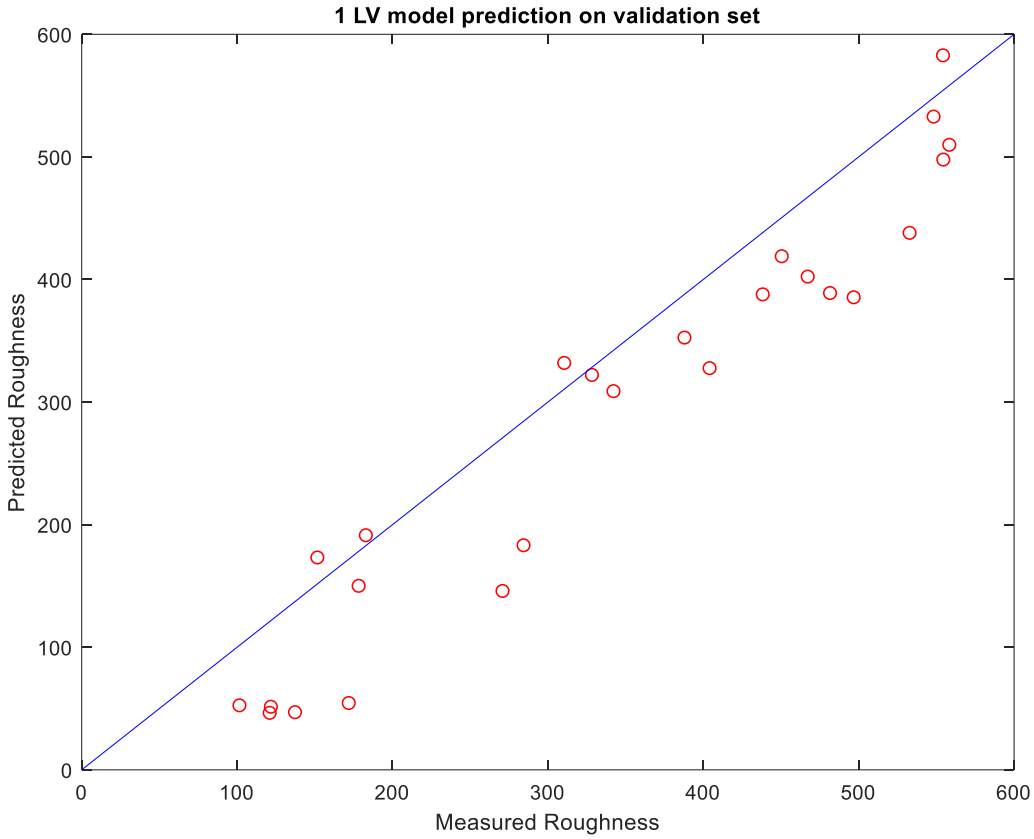

S12: Multivariate PLS model constructed on second derivative spectra to predict surface roughness S_a. R^2 = 0.82.